SANDIA REPORT
SAND2020-10555
Printed September 2020

Sandia National Laboratories

Simulation Analysis of Geometry and Material Effects for Dropkinson Bar

Constantin Brif and Andrew J. Stershic

Prepared by
Sandia National Laboratories
Albuquerque, New Mexico
87185 and Livermore, California
94550

Issued by Sandia National Laboratories, operated for the United States Department of Energy by National Technology & Engineering Solutions of Sandia, LLC.

Available to DOE and DOE contractors from
U.S. Department of Energy
Office of Scientific and Technical Information
P.O. Box 62
Oak Ridge, TN 37831

Telephone: (865) 576-8401
Facsimile: (865) 576-5728
E-Mail: reports@osti.gov
Online ordering: http://www.osti.gov/scitech

Available to the public from
U.S. Department of Commerce
National Technical Information Service
5301 Shawnee Rd
Alexandria, VA 22312

Telephone: (800) 553-6847
Facsimile: (703) 605-6900
E-Mail: orders@ntis.gov
Online order: https://classic.ntis.gov/help/order-methods/

ABSTRACT

The reported research is motivated by the need to address a key issue affecting the Dropkinson bar apparatus. This unresolved issue is the interference of the stress wave reflected from the bar–beam boundary with the measurement of the stress–strain response of a material tested in the apparatus. The purpose of the wave beam that is currently connected to the bar is to dissipate the stress wave, but the portion of the wave reflected from the bar–beam boundary is still significant. First, we focused on understanding which parameters affect the reflected wave's arrival time at a strain gauge. Specifically, we used finite-element numerical simulations with the Sierra/SM module to study the effects of various bar–beam connection fixities, alternative wave beam materials, and alternative geometries of the Dropkinson bar system based on a monolithic design. The conclusion of this study is that a partial reflection always occurs at the bar–beam boundary (or, for a monolithic design, at a point where the bar geometry changes). Therefore, given a fixed total length of the bar, it is impossible to increase the reflected wave's arrival time by any significant amount.

After reaching this conclusion, we focused instead on trying to minimize the energy of the reflected stress wave circulating up and down through the bar over a relatively long period of time (10 ms). Once again, we used numerical simulations with the Sierra/SM module to investigate the effects of various bar–beam connection fixities, alternative wave beam materials, and parameters of an asymmetric monolithic design of the bar-and-beam system. This study demonstrated that various parameters can significantly affect the energy of the wave reflections, with the difference between best and worst configurations being about one order of magnitude in terms of energy.

Based on the obtained results, we conclude with concrete takeaways for Dropkinson bar users and propose potential directions for future research and optimization.

ACKNOWLEDGEMENTS

The authors thank Brett Sanborn, Bo Song, and Colin Loeffler for providing detailed information about the Dropkinson bar apparatus and intermediate strain rate experiments.

CONTENTS

1. Introduction 10
   1.1. Dropkinson bar system 10
   1.2. Problem description and study scope 11
2. Model properties 12
   2.1. Longitudinal vibrations in a thin bar 12
   2.2. Reflection and transmission at a boundary 12
   2.3. Properties of the Hopkinson bar 13
3. Simulation approach 14
4. Investigation of wave reflection time 16
   4.1. Computation of the reflected wave's round trip time 16
   4.2. Comparing wave reflection times for a perfect connection 16
   4.3. Comparing wave reflection times for different bar–beam connections 17
   4.4. Comparing wave reflection times for different wave beam materials 18
   4.5. Monolithic design of the Dropkinson bar 20
5. Investigation of reflected wave energy 27
   5.1. Computation of the energy ratio 27
   5.2. Comparing energy ratios for different bar–beam connections 27
   5.3. Comparing energy ratios for different wave beam materials 29
   5.4. Varying both the bar–beam connection and the wave beam material 31
   5.5. Asymmetric monolithic design of the Dropkinson bar 34
      5.5.1. Dependence of energy ratio on beam delta 36
      5.5.2. Dependence of energy ratio on radius of bar curvature 37
      5.5.3. Dependence of energy ratio on beam top radius 39
      5.5.4. Dependence of energy ratio on beam delta and average beam thickness for optimal value of radius of bar curvature 41
      5.5.5. Dependence of energy ratio on beam length 43
      5.5.6. Examples of stress wave propagation 44
6. Summary and conclusions 45

LIST OF FIGURES

Figure 1-1. Dropkinson bar. Right top: Schematic of test configuration. Left: Sierra model of stress waves (frontal view). Right bottom: Sierra model of wave beam and bar–beam connection. 10
Figure 3-1. Sierra/SD simulation of stress wave propagation in Dropkinson bar without wave beam: first non-rigid mode and first longitudinal mode. 14
Figure 3-2. Sierra/SD simulation of stress wave propagation in Dropkinson bar connected to wave beam: first mode and first bending (vertical only) mode. 15
Figure 4-1. Examples of perfect bar connections. 16
Figure 4-2. Simulated stress wave propagation (raw force signal), for the free and fixed perfect connections and for the bar connected to the wave beam. 17
Figure 4-3. Simulated stress wave propagation (filtered force signal), for 18 variants of the bar–beam connection. 18
Figure 4-4. Simulated stress wave propagation (raw force signal), for AISI 4140 and three hypothetical wave beam materials. 19

Figure 4-5. WRT versus cfactor for 660 hypothetical wave beam materials. 20
Figure 4-6. Symmetric monolithic design (SMD) of the bar-and-beam system. 21
Figure 4-7. Simulated stress wave propagation (raw force signal), for the SMD with three different sets of parameters. 22
Figure 4-8. Simulated stress wave propagation (filtered force signal), for the SMD with three different sets of parameters. 22
Figure 4-9. Simulated stress wave propagation (filtered force signal), for the SMD with r = 1" 23
Figure 4-10. WRT versus beam, support, and overhang parameters, for the SMD with r = 1" 23
Figure 4-11. Simulated stress wave propagation (filtered force signal), for the SMD with r = 42" .. 24
Figure 4-12. WRT versus beam, support, and overhang parameters, for the SMD with r = 42" 24
Figure 4-13. Simulated stress wave propagation (filtered force signal), for the SMD with r = 72" .. 25
Figure 4-14. WRT versus beam, support, and overhang parameters, for the SMD with r = 72" 25
Figure 4-15. WRT versus r, for the SMD with Lbeam = 1", Lsupp = Lover = 36" 26
Figure 5-1. Simulated stress wave propagation (filtered force signal) over 10 ms, for three connection variants. 29
Figure 5-2. Energy ratio ER versus cfactor for 660 hypothetical wave beam materials, color coded by a range of Zfactor values. 30
Figure 5-3. Energy ratio ER versus Zfactor for 660 hypothetical wave beam materials, color coded by a range of cfactor values. 30
Figure 5-4. Simulated stress wave propagation (filtered force signal) over 10 ms, for three hypothetical wave beam materials. 31
Figure 5-5. Energy ratio ER versus cfactor for connection variants 0, 9, 17, 4 and various hypothetical wave beam materials. 33
Figure 5-6. Simulated stress wave propagation (filtered force signal) over 10 ms, for connection variant 0 with Material X and connection variant 17 with Material Y. 34
Figure 5-7. Asymmetric monolithic design (AMD) of the bar-and-beam system. 34
Figure 5-8. Views of the AMD model geometry. 35
Figure 5-9. Energy ratio ER and WRT tWR versus Δbeam for AMD with rbtop = Δbeam and fixed values of other parameters. 36
Figure 5-10. Energy ratio ER versus Δbeam for AMD with various values of rbtop and fixed values of other parameters. 37
Figure 5-11. Energy ratio ER versus r for AMD with four parameter value combinations. 38
Figure 5-12. WRT tWR versus r for AMD with four parameter value combinations. 38
Figure 5-13. Energy ratio ER and WRT tWR versus r for AMD with rbtop = 10" and combination (d) of other parameter values. 39
Figure 5-14. Energy ratio ER and WRT tWR versus rbtop for AMD with r = 19.1" and combination (d) of other parameter values. 40
Figure 5-15. Energy ratio ER versus rbtop for AMD with three different values of r and combination (d) of other parameter values. 40
Figure 5-16. Energy ratio ER and WRT tWR versus the ratio Δbeamr for AMD with r = 19.1" and rbtop = 10" 41
Figure 5-17. Energy ratio ER and WRT tWR versus Lbeam for AMD with r = 19.1" and rbtop = 10". 42
Figure 5-18. Energy ratio ER and WRT tWR versus Lbeam for AMD with r = 15.1" and rbtop = 10". 42

Figure 5-19. Energy ratio ER versus Lsupp for AMD with four different values of Lsupp + Lover. 43
Figure 5-20. Simulated stress wave propagation (filtered force signal) over 10 ms, for AMD with three different sets of parameter values. 44

LIST OF TABLES

Table 1-1. Materials of the Dropkinson bar components. 10
Table 4-1. Variants of the bar–beam connection. 17
Table 4-2. Parameters of the symmetric monolithic design (SMD) of the bar-and-beam system. 21
Table 5-1. Wave reflection times and energy ratios for AISI 4140 steel and 18 variants of the bar–beam connection. 28
Table 5-2. Properties of Material X and Material Y. 31
Table 5-3. Energy ratios for Material X and 18 variants of the bar–beam connection 32
Table 5-4. Parameters of the asymmetric monolithic design (AMD) of the bar-and-beam system. .. 35

This page left blank

ACRONYMS AND DEFINITIONS

Abbreviation	Definition
WRT	wave reflection time
SMD	symmetric monolithic design
AMD	asymmetric monolithic design
BTR	beam top radius

1. INTRODUCTION

1.1. Dropkinson bar system

The Hopkinson bar (also known as split-Hopkinson pressure bar or Kolsky bar) [1],[2], is an apparatus for testing the dynamic stress–strain response of materials [3]. An apparatus used in Sandia utilizes a vertically falling bar and is referred to as the "Dropkinson" bar [4],[5]. Figure 1-1 shows a schematic of the Dropkinson bar test configuration along with the Sierra model [6], including the bar, the wave beam, and the bar–beam connection. The model components include: Hopkinson bar, wave beam, nut plate, nut, screws, and supports. Materials of the components are described in Table 1-1.

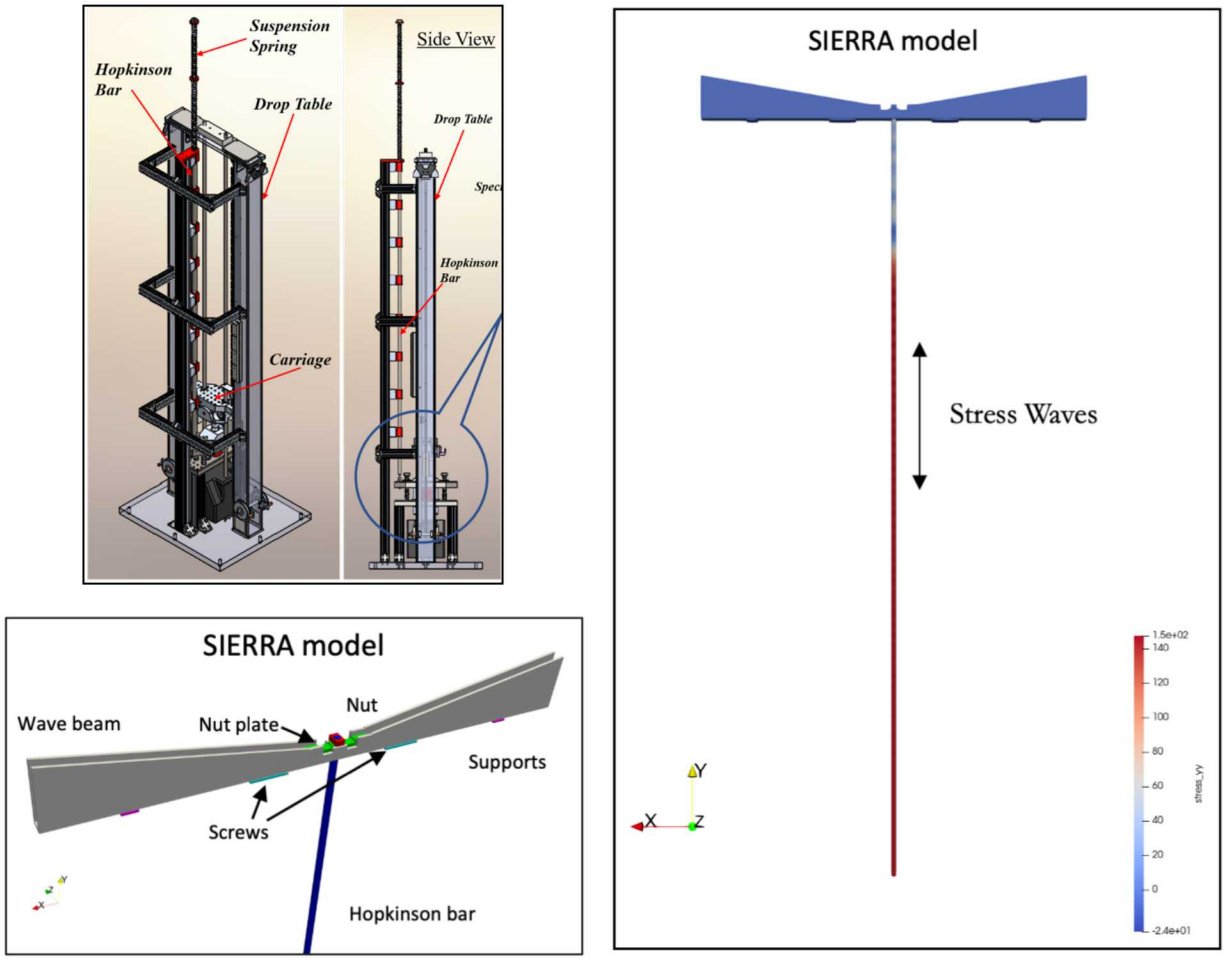

Figure 1-1. Dropkinson bar. Right top: Schematic of test configuration. Left: Sierra model of stress waves (frontal view). Right bottom: Sierra model of wave beam and bar–beam connection.

Table 1-1. Materials of the Dropkinson bar components.

Component(s)	Material
Hopkinson bar	Steel C300
Wave beam, nut plate, nut, screws	Steel AISI 4140
Supports	Aluminum 6061-T5

1.2. Problem description and study scope

This research is based on data provided by the DE experimental partners in Org. 1528, including Brett Sanborn, Bo Song, and Colin Loeffler. The key issue is that the stress wave reflected down from the bar–beam boundary interferes with the measurement of the stress–strain response of a material that is being tested in the Dropkinson bar apparatus. The purpose of the wave beam that is currently connected to the Hopkinson bar is to dissipate the stress wave [7], but the portion of the wave reflected from the bar–beam boundary is still significant.

At the onset of this study, we formulated the following objectives:

- Investigate signal as a function of design parameters
  - Which parameters determine the stress wave reflection?
- Investigate contact condition
  - Does an imperfect connection cause the stress wave reflection?
- Improve beam design
  - Extend the measurement period by slowing down the stress wave reflection

In the first part of the performed research, we focused on understanding which parameters affect the reflected wave's arrival time at a strain gauge (located 1 ft above the bottom end of the bar). Specifically, we used finite-element numerical simulations with the Sierra/SM module [6] to study the effects of various bar–beam connection fixities, alternative wave beam materials, and alternative geometries of the Dropkinson bar system based on a monolithic design. The conclusion of this study was that a partial reflection always occurs at the bar–beam boundary (or, for a monolithic design, at a point where the bar geometry changes), and therefore, given a fixed total length of the bar, it is impossible to increase the reflected wave's arrival time by any significant amount.

In the second part of the performed research, we focused instead on trying to minimize the energy of the reflected stress wave circulating up and down through the bar over a relatively long period of time (10 ms). Once again, we used numerical simulations with the Sierra/SM module to investigate the effects of various bar–beam connection fixities, alternative wave beam materials, and parameters of an asymmetric monolithic design of the bar-and-beam system. The conclusion of this study is that various parameters can significantly affect the energy of the reflected wave, with the difference between best and worst configurations being about one order of magnitude.

2. MODEL PROPERTIES

2.1. Longitudinal vibrations in a thin bar

The wave equation for a displacement $w = w(x,t)$ is

$$\frac{\partial^2 w}{\partial t^2} = c\frac{\partial^2 w}{\partial x^2},$$

where c is the velocity of the longitudinal wave (the same as the sound velocity): $c = \sqrt{E/\rho}$, E is Young's modulus and ρ is the density (the mass per unit volume) of the bar material. The general solution of the wave equation has the form:

$$w(x,t) = w_1(ct - x) + w_2(ct + x).$$

The normal modes of vibration depend on boundary conditions at the bar ends. For a bar of length L, if both ends are fixed, or if both ends are free, the mode frequencies are given by

$$f_n = n\frac{c}{2L}, \quad n = 1,2,3, \ldots$$

and for a bar fixed at one end and free at the other,

$$f_m = m\frac{c}{4L}, \quad m = 1,3,5, \ldots.$$

2.2. Reflection and transmission at a boundary

When a wave crosses a boundary of two different materials, a portion of the wave is transmitted and another portion is reflected. Consider a wave that propagates in material 1 and arrives at the boundary with material 2. We denote the amplitudes of the incident, transmitted, and reflected waves as w_i, w_t, and w_r, respectively. The relationship between these amplitudes is [8],[9]

$$w_t = \frac{2Z_1}{Z_1 + Z_2} w_i,$$

$$w_r = \frac{Z_1 - Z_2}{Z_1 + Z_2} w_i.$$

The quantity Z is known as the impedance (correspondingly, Z_1 and Z_2 are impedances for materials 1 and 2, respectively). In general, the impedance is the force divided by the velocity. The impedance for longitudinal waves in an infinitely long bar is

$$Z = \mu c = \rho c A = \sqrt{E\rho}A,$$

where $\mu = \rho A$ is the mass per unit length and A is the cross-sectional area of the bar.

It follows from the relationship between w_i and w_r that the amplitude of the reflected wave is zero if the impedances for the two materials are equal ($Z_1 = Z_2$). Note that a reflection will occur at any boundary where the impedance changes. This can be caused by a change of material properties (e.g., a boundary between materials with different E and/or ρ values) or by a change in geometry of a homogeneous object (e.g., a location where the cross-sectional area of the bar changes).

2.3. Properties of the Hopkinson bar

The Hopkinson bar is a cylinder of radius 0.5" (0.0127 m) and height 12 ft (3.6576 m). Due to these dimensions, the thin bar model should provide a good approximation. The bar is made of Maraging C300 steel. The bar properties are:

- Density: $\rho = 0.289$ lbs./cu.in. $= 8.0$ g/cm^3 $= 8000.0$ kg/m^3
- Young's modulus: $E = 27.54 \times 10^6$ psi $= 1.899 \times 10^{11}$ Pa $= 189.9$ GPa
- Longitudinal wave speed (using the thin bar model): $c = 4872.1$ m/s
- Frequency of first longitudinal mode (using the thin bar model): $f_1 = 666.024$ Hz
- Wave round-trip traveling time (using the thin bar model, for a strain gauge located 1 ft above the bottom end of the bar): $t_{\mathrm{RW}} = 0.001376$ s
- Cross-sectional area: $A = 0.7854$ sq.in. $= 5.067$ cm^2 $= 5.067 \times 10^{-4}$ m^2
- Impedance per unit area (using the thin bar model): $z = \frac{Z}{A} = 3.898 \times 10^7$ kg/(m^2 s)
- Impedance (using the thin bar model): $Z = 1.975 \times 10^4$ kg/s

3. SIMULATION APPROACH

First, we investigated whether it is possible to quantify the stress wave reflection time with structural dynamics analysis in the Sierra/SD module [6]. Our first question was: does the stress wave reflection time correspond to the first longitudinal mode of the bar or the first (vertical-only) bending mode of the wave beam?

We started by simulating the stress wave propagation in the Hopkinson bar without the wave beam (see **Error! Reference source not found.**), using both Sierra/SD and Sierra/SM modules. Considering the wave round-trip traveling time for a strain gauge located 1 ft above the bottom end of the bar, we obtained the following results:

- Sierra/SD simulation:
  - First non-rigid mode frequency is 81.3 Hz
  - First longitudinal mode frequency is 739.9 Hz; wave round-trip traveling time is 1.35 ms
- Sierra/SM simulation:
  - Wave round-trip traveling time is 1.36 ms

Based on these results, the Sierra/SD prediction (for the first longitudinal mode) and the Sierra/SM prediction agree, and also they both agree with the wave round-trip traveling time observed in the experiment.

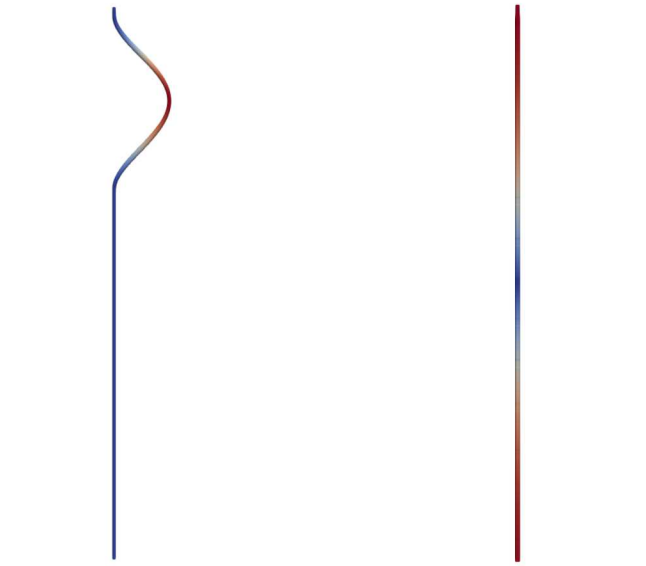

Figure 3-1. Sierra/SD simulation of stress wave propagation in Dropkinson bar without wave beam: first non-rigid mode and first longitudinal mode.

Next, we simulated the stress wave propagation in the Hopkinson bar connected to the wave beam (see Figure 3-2), using both Sierra/SD and Sierra/SM modules. Considering the wave round-trip traveling time for a strain gauge located 1 ft above the bottom end of the bar, we obtained the following results:

- Sierra/SD simulation:
  - First mode frequency is 36.9 Hz
  - First bending mode frequency is 59.6 Hz; wave round-trip traveling time is 16.78 ms
- Sierra/SM simulation:
  - Wave round-trip traveling time is 1.36 ms

Based on these results, the Sierra/SD prediction (for the first bending mode) and the Sierra/SM prediction do not agree. The Sierra/SM result for the stress wave round-trip traveling time agrees with the experiment and is not affected by the presence or absence of the wave beam (which indicates that the reflection happens at the bar–beam boundary). On the other hand, the Sierra/SD prediction for the stress wave round-trip traveling time, derived from the wave beam's bending mode, disagrees with the experiment. Therefore, simulations with the Sierra/SD module cannot be reliably used to compute the stress wave reflection time. In the remainder of this report, all results are obtained using dynamic simulations with the Sierra/SM module.

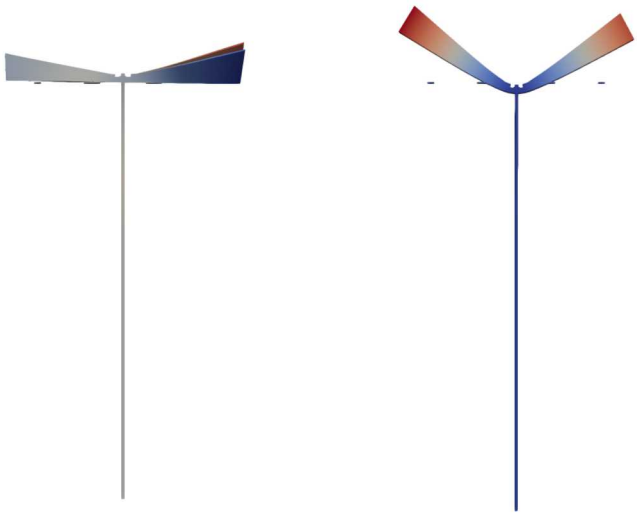

Figure 3-2. Sierra/SD simulation of stress wave propagation in Dropkinson bar connected to wave beam: first mode and first bending (vertical only) mode.

4. INVESTIGATION OF WAVE REFLECTION TIME

4.1. Computation of the reflected wave's round trip time

The time interval of interest is the round-trip traveling time of the reflected stress wave, measured at a strain gauge located 1 ft above the bottom end of the bar. For the sake of simplicity, we will refer to this time interval as the wave reflection time (WRT). It is defined as

$$t_{\mathrm{WR}} = t_{\mathrm{rws}} - t_{\mathrm{iws}}, \tag{1}$$

where t_{iws} is the start time of the initial wave (i.e., the time at which the initial wave arrives at the gauge) and t_{rws} is the start time of the reflected wave (i.e., the time at which the reflected wave arrives at the gauge). These times are computed by using the following threshold conditions:

- t_{iws} is the first time when $|f_{\mathrm{filt}}| \geq 0.5$ lbf for $t < 0.5$ ms
- t_{rws} is the first time when $|f_{\mathrm{filt}}| \geq 0.5$ lbf for $t \geq 0.5$ ms

Here, f_{filt} is the filtered stress force, obtained from the raw stress force f by applying a 5th-order filter with a pass frequency of 10 kHz at data interpolated to a time step of 1.0e-8 s.

4.2. Comparing wave reflection times for a perfect connection

We begin by considering a number of scenarios in which the top end of the Hopkinson bar is perfectly connected to a spring made of the same material as the bar (i.e., with the same density ρ) and with a spring constant k. Specific examples include the cases when the top end of the bar is free ($k = 0$) or fixed ($k \to \infty$), as shown in Figure 4-1.

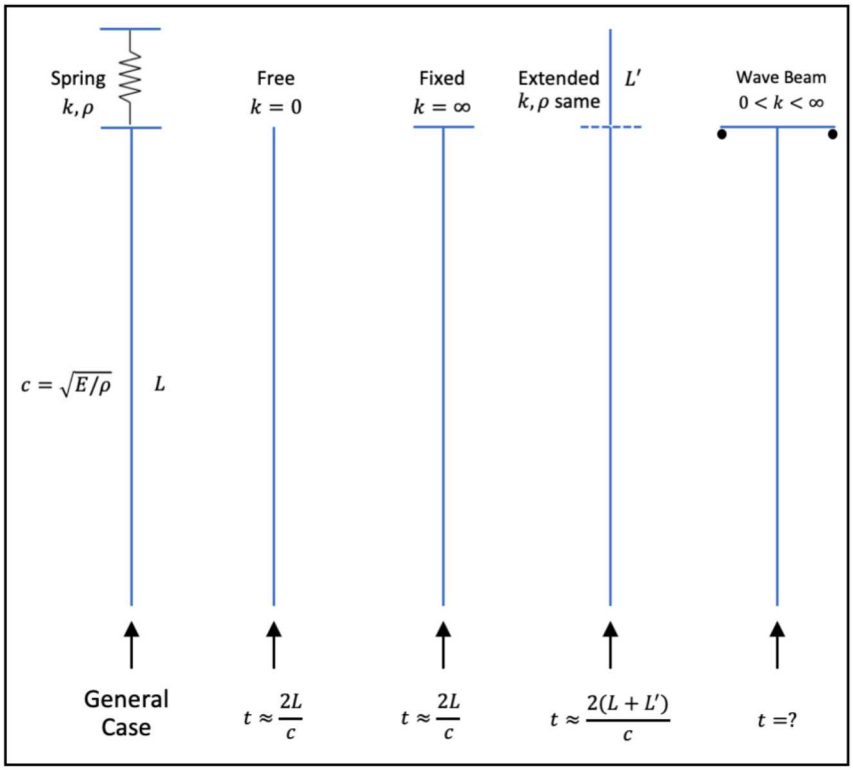

Figure 4-1. Examples of perfect bar connections.

We simulated the stress wave propagation for the free and fixed perfect connections of the bar, and computed the respective WRTs. The simulation results agree with the analytical prediction. The WRT obtained for the bar connected to the wave beam is not significantly different and matches the experimentally measured time (~ 1.3 ms), as shown in Figure 4-2. The conclusion is that the stress wave partially reflects from the top end of the bar whether it is connected to the wave beam or not.

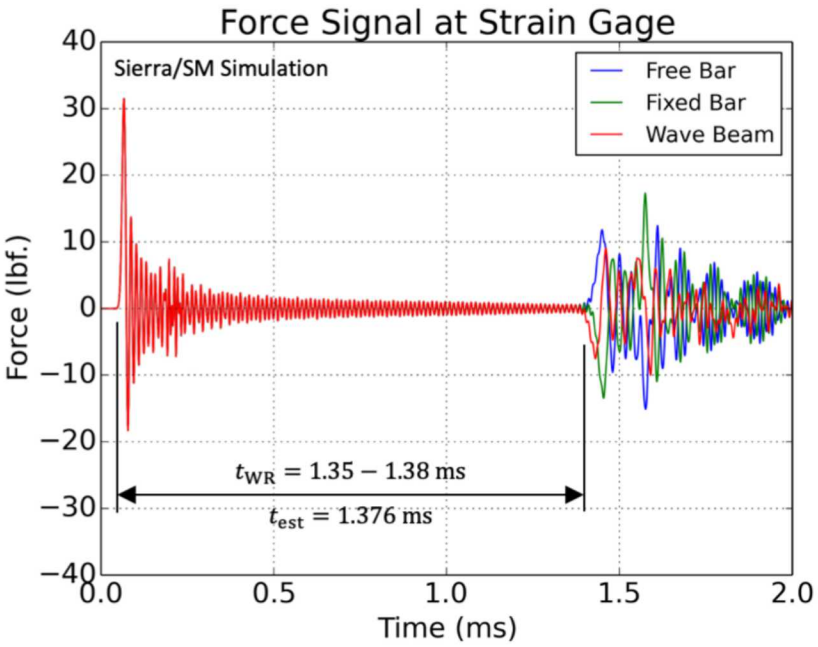

Figure 4-2. Simulated stress wave propagation (raw force signal), for the free and fixed perfect connections and for the bar connected to the wave beam.

4.3. Comparing wave reflection times for different bar–beam connections

Next, we investigated whether changing the bar–beam connection quality details affects the WRT. Specifically, we varied connection fixity at various locations (see the lower left panel of Figure 1-1), which resulted in 18 different connection variants (labeled from 0 to 17), shown in Table 4-1. In Table 4-1, T stands for "Tied" (welded or securely threaded) and F stands for "Frictional" (sliding). Note that variant 0 is implemented in the current experiment, and therefore we use it as the default one in the rest of the studies where the bar–beam connection is fixed.

Table 4-1. Variants of the bar–beam connection.

Compo-nent	0	1	2	3	4	5	6	7	8	9	10	11	12	13	14	15	16	17
Bar / Nut Plate	T	T	T	T	T	T	T	T	F	F	F	F	F	F	F	F	F	T
Bar / Nut	T	T	T	T	F	F	F	F	T	T	T	T	F	F	F	F	F	T
Nut Plate / Nut	T	T	F	F	T	T	F	F	T	T	F	F	T	T	F	F	F	T
Nut Plate / Beam	T	F	T	F	T	F	T	F	T	F	T	F	T	F	T	F	F	T
Bar / Beam	F	F	F	F	F	F	F	F	F	F	F	F	F	F	F	F	T	T

We simulated the stress wave propagation for the 18 variants of the bar–beam connection, and computed the respective WRTs. The resulting filtered force signals are shown in Figure 4-3. We find that the WRT values for all 18 variants are very similar (see Table 5-1 below). The smallest observed value of the WRT (1.356 ms) is obtained for variant 17 (TTTTT), and the largest observed value of the WRT (1.389 ms) is obtained for variants 10 (FTFTF) and 11 (FTFFF). Therefore, we conclude that changing connection details has only minor influence on the WRT. On the other hand, we note that connection details have a significant effect on the reflected wave amplitude (see further discussion in section 5.2).

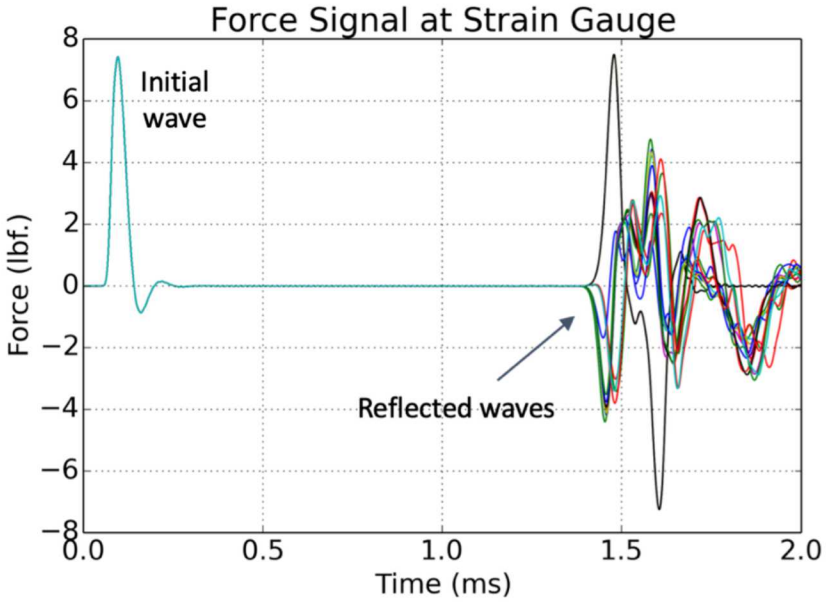

Figure 4-3. Simulated stress wave propagation (filtered force signal), for 18 variants of the bar–beam connection.

4.4. Comparing wave reflection times for different wave beam materials

Next, we investigated whether changing the properties of the wave beam material affects the WRT.[1] Specifically, we simulated the stress wave propagation for 66 hypothetical wave beam materials with varying values of the density ρ and Young's modulus E (up to two orders of magnitude larger or smaller than those of AISI 4140). The resulting values of the sound velocity, $c = \sqrt{E/\rho}$, varied from 0.022 to 89 times that of AISI 4140. In all these simulations, the wave beam geometry was fixed (see Figure 1-1) and the bar–beam connection was also fixed (variant 0 in Table 4-1).

The resulting raw force signals are shown in Figure 4-4, for four wave beam materials: AISI 4140 (the actual material) and three hypothetical materials. Each of the hypothetical materials is labeled by the value of c_{factor}, defined as the ratio of the sound velocity c in the material to that in AISI 4140: $c_{\text{factor}} = \frac{c}{c_{4140}}$. We see that the WRT values are very similar for all studied wave beam materials

[1] This analysis was performed in order to draw preliminary conclusions about the sensitivity of the WRT to the beam design. In this sense, changing the beam material serves as a proxy for changing the beam geometry, in that both affect the frequency response and the impedance. If the WRT is sensitive to beam material changes, then beam geometry design (maintaining the original AISI 4140 material) could be also effective in modifying the WRT. If the WRT is insensitive to beam material changes, then changes to the beam geometry will be unlikely to affect the WRT. From the numerical point of view, performing parameter studies on two material parameters is far more cost-efficient than analyzing a parametrized wave beam geometry.

(AISI 4140 and 66 hypothetical materials), despite a very significant variation in their properties. Since the WRT is practically independent of the wave beam material, we conclude that it is almost exclusively determined by the partial reflection of the stress wave from the bar–beam boundary.

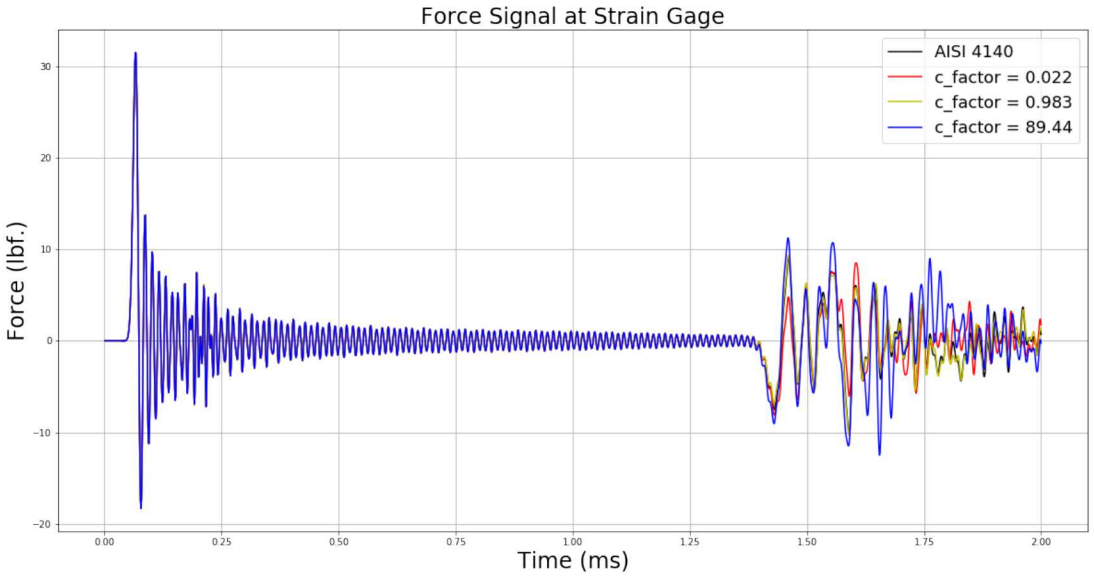

Figure 4-4. Simulated stress wave propagation (raw force signal), for AISI 4140 and three hypothetical wave beam materials.

To more carefully investigate the variation of the WRT, we also performed an additional set of simulations for 660 hypothetical wave beam materials with c_{factor} values ranging from 0.01 to 80. The resulting dependence of the WRT on c_{factor} is shown in Figure 4-5, where dots are color-coded by a range of Z_{factor} values, where $Z_{\text{factor}} = \frac{Z}{Z_{4140}}$ is the ratio of the impedance $Z \propto \sqrt{E\rho}$ for the hypothetical material to that for AISI 4140. We see that the WRT varies very insignificantly, between 1.356 and 1.363, with a larger impedance typically corresponding to a smaller t_{WR}.

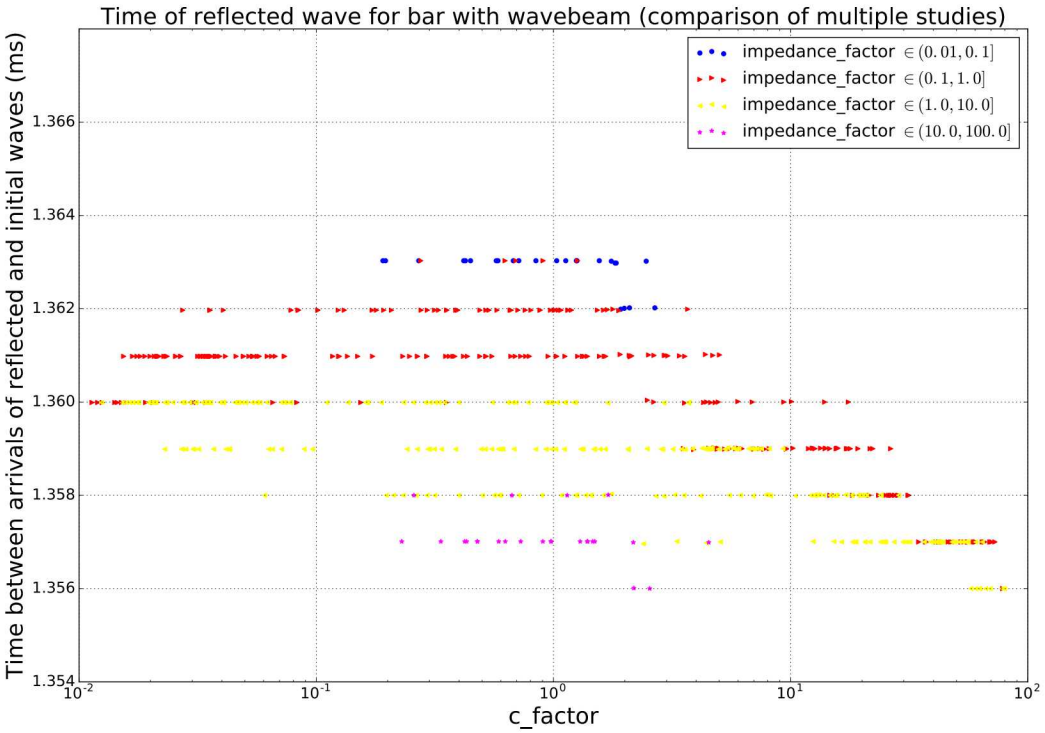

Figure 4-5. WRT versus $c_{\mathbf{factor}}$ for 660 hypothetical wave beam materials.

4.5. Monolithic design of the Dropkinson bar

Based on the results of studies described in sections 4.2–4.4, we understood that the stress wave is partially reflected from the bar–beam boundary. Therefore, we investigated whether it is possible to eliminate or significantly reduce the reflection by using a monolithic design (i.e., no boundary between the bar and the beam). The proposed symmetric monolithic design (SMD) of the bar-and-beam system is shown in Figure 4-6 and its parameters are described in Table 4-2. We assume that the monolithic bar-and-beam system is made of Maraging C300 steel.

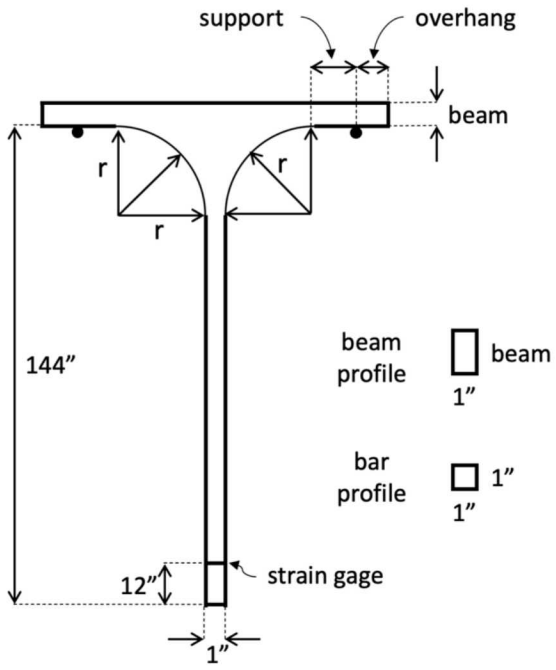

Figure 4-6. Symmetric monolithic design (SMD) of the bar-and-beam system.

Table 4-2. Parameters of the symmetric monolithic design (SMD) of the bar-and-beam system.

Parameter	Notation	Description
r	r	radius of bar curvature
beam	L_{beam}	beam thickness
support	L_{supp}	distance from r to support
overhang	L_{over}	distance past support

We simulated the stress wave propagation for the SMD, for various values of four parameters: r (r), L_{beam} (beam), L_{supp} (support), and L_{over} (overhang). We discovered that the signal characteristics are mostly affected by the r parameter. Figure 4-7 and Figure 4-8 show, respectively, raw and filtered force signals for three representative simulations with small ($r = 1.104''$), medium ($r = 41.490''$) and large ($r = 71.971''$) values of r.

We see that the WRT changes, depending on the value of r. Specifically, the WRT decreases as r increases. A logical explanation for this effect is that for a larger r the widening of the bar begins at a lower point, and this change of the bar geometry (which leads to the associated change of the impedance) causes a partial reflection of the stress wave, resulting in an earlier arrival time of the reflected wave at the strain gauge. Also, the amplitude of the reflected wave decreases as r increases. This is likely due to the fact that for a larger r the change of the bar width (and, consequently, the change of the impedance) is more gradual, and therefore the partial reflection is weaker.

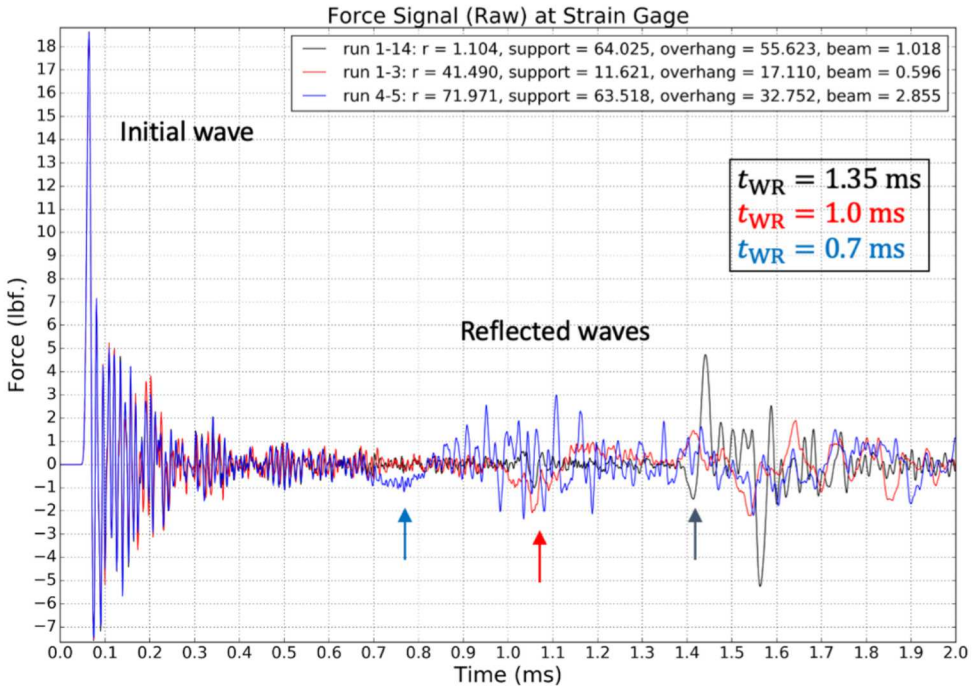

Figure 4-7. Simulated stress wave propagation (raw force signal), for the SMD with three different sets of parameters.

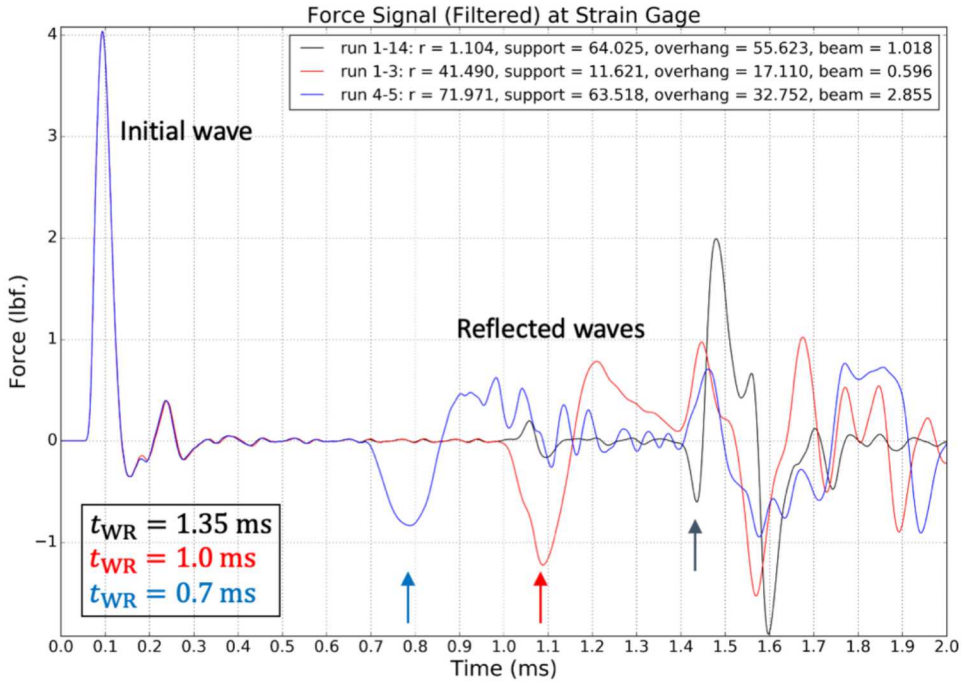

Figure 4-8. Simulated stress wave propagation (filtered force signal), for the SMD with three different sets of parameters.

Figure 4-9 shows typical results for the filtered force signal for the SMD with $r = 1''$. While the WRT is practically constant when r is fixed, the amplitude of the reflected wave varies significantly depending on the value of L_{beam}, with a larger L_{beam} value resulting in a weaker reflection. Also, the amplitude of the reflected wave changes its sign between $L_{\text{beam}} < 1''$ and $L_{\text{beam}} > 1''$.

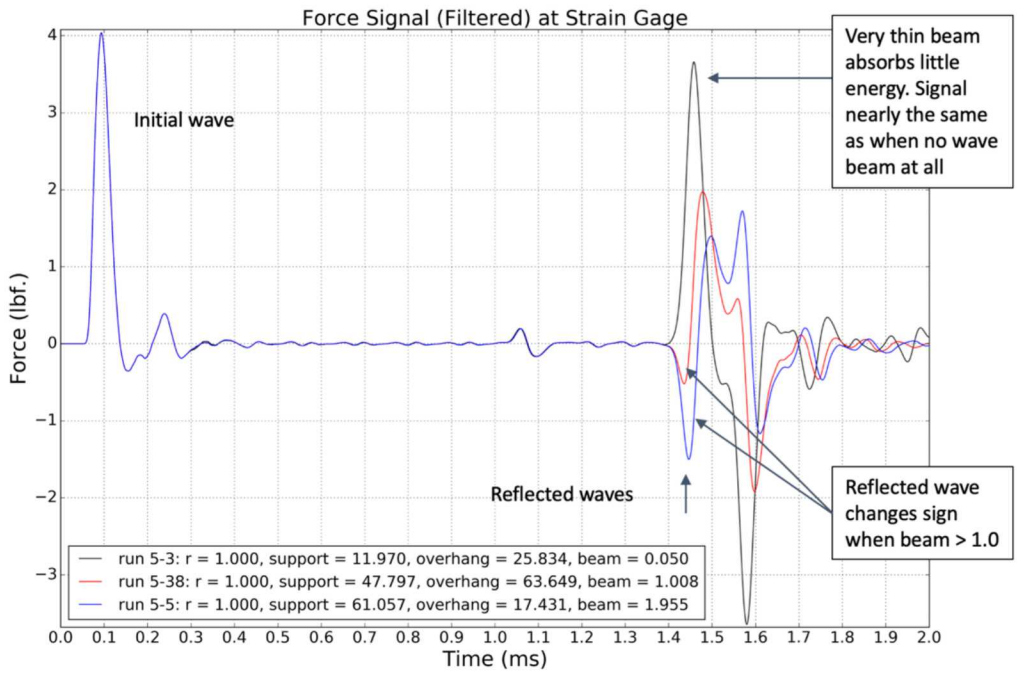

Figure 4-9. Simulated stress wave propagation (filtered force signal), for the SMD with $r = 1''$.

We performed additional simulations to investigate the WRT dependence on the beam, support, and overhang parameters, for the SMD with $r = 1''$. These results are shown in Figure 4-10, where the WRT is plotted against each of the three variable parameters. We see that the WRT varies very insignificantly (between 1.356 ms and 1.386 ms), and the only trend is with respect to the L_{beam} value. The discontinuity in the WRT trend at $L_{\text{beam}} = 1''$ is likely related to the sign change of the reflected wave amplitude at the same L_{beam} value.

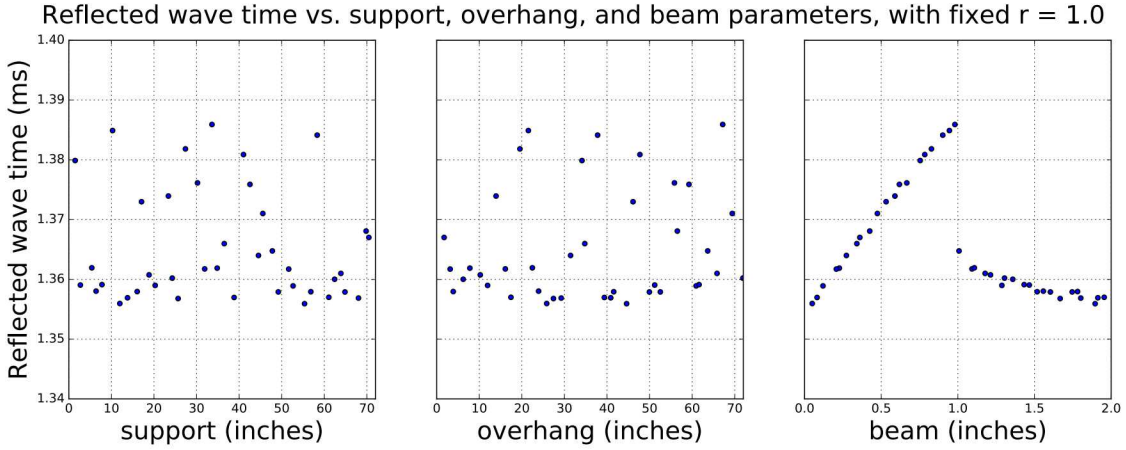

Figure 4-10. WRT versus beam, support, and overhang parameters, for the SMD with $r = 1''$.

We also performed similar analyses for the SMD with $r = 42''$ and $r = 72''$. For $r = 42''$, typical filtered force signals are shown in Figure 4-11 and the WRT dependence on beam, support, and overhang is shown in Figure 4-12. For $r = 72''$, typical filtered force signals are shown in Figure 4-13 and the WRT dependence on beam, support, and overhang is shown in Figure 4-14. We find

that, for medium to large r values, reflection of the stress wave is almost completely determined by the r parameter. No significant variation with respect to other three parameters is observed.

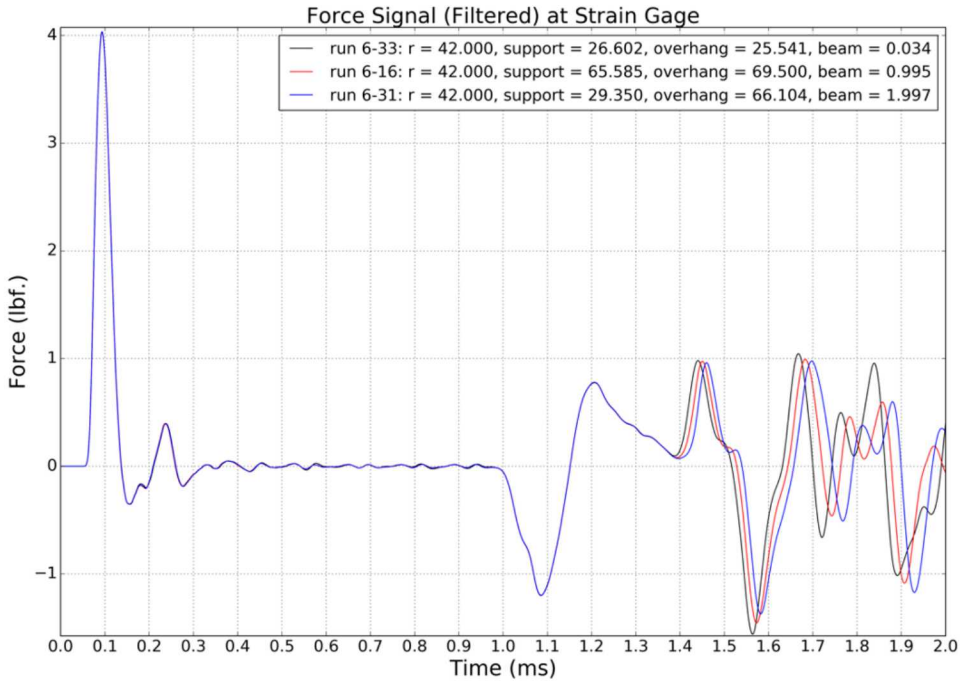

Figure 4-11. Simulated stress wave propagation (filtered force signal), for the SMD with $r = 42$".

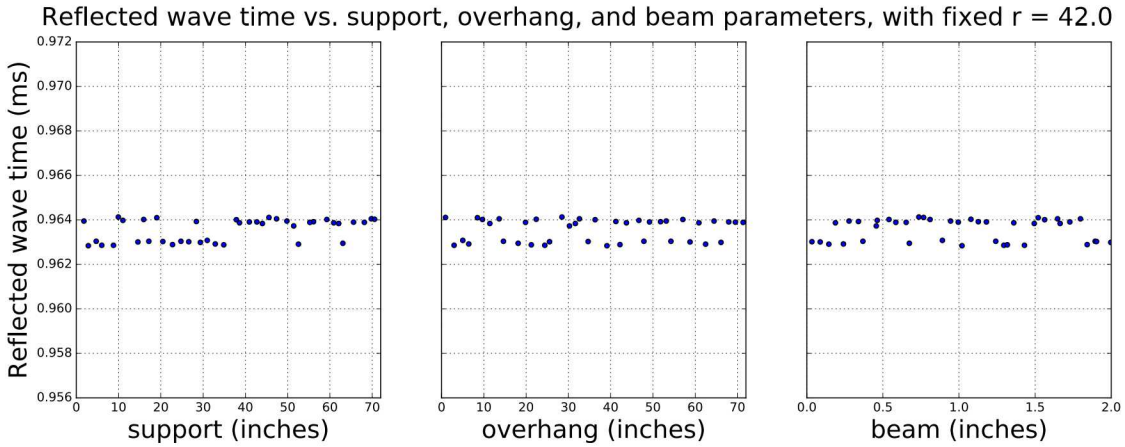

Figure 4-12. WRT versus beam, support, and overhang parameters, for the SMD with $r = 42$".

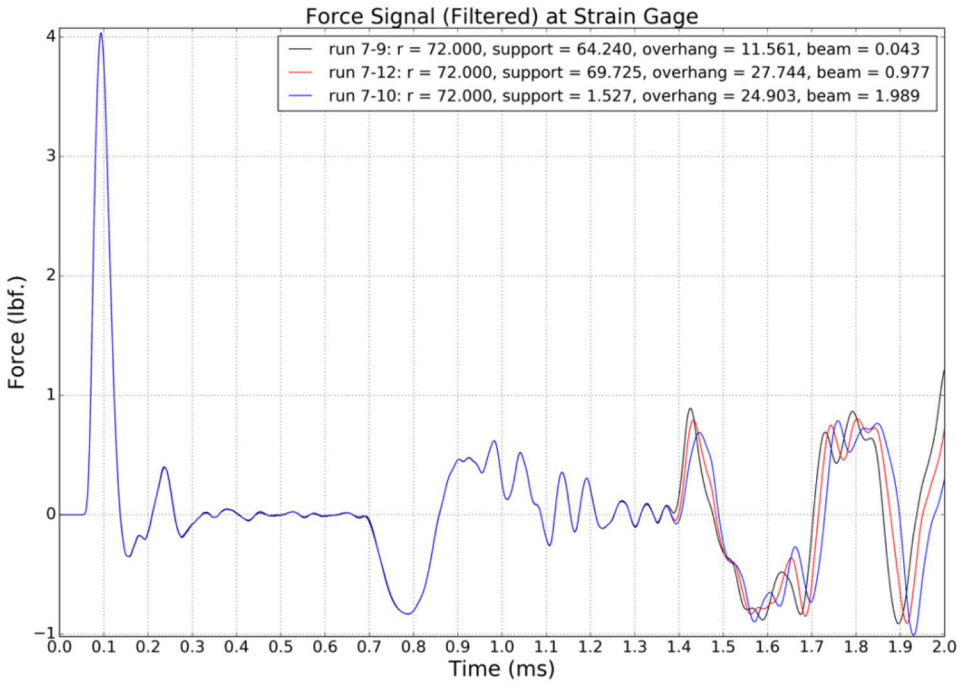

Figure 4-13. Simulated stress wave propagation (filtered force signal), for the SMD with $r = 72''$.

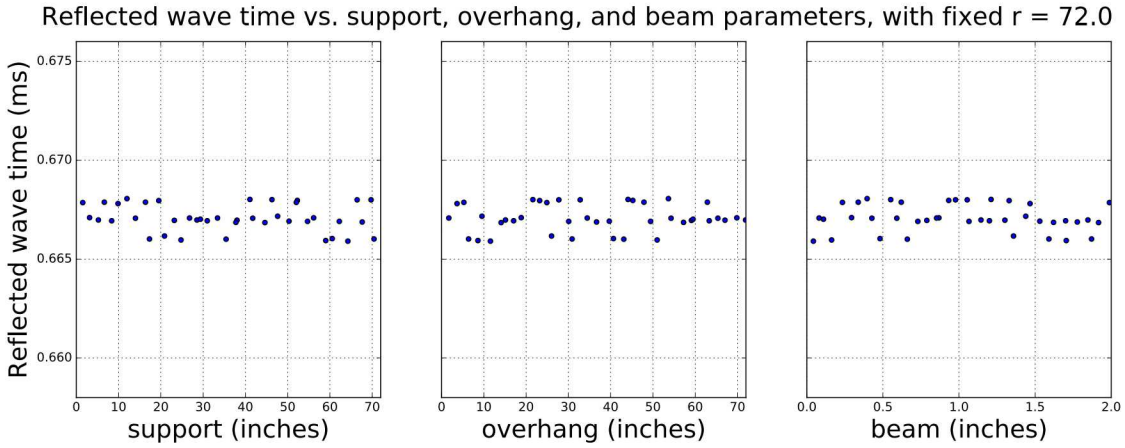

Figure 4-14. WRT versus beam, support, and overhang parameters, for the SMD with $r = 72''$.

As discussed above, we observed that the WRT decreases as the r value increases. We performed additional simulations to investigate this dependence. These results are shown in Figure 4-15, where the WRT is plotted against r, with fixed values of other three parameters ($L_{\text{beam}} = 1''$, $L_{\text{supp}} = 36''$, and $L_{\text{over}} = 36''$). We see that the trend of the WRT dependence on r closely follows the theoretical prediction based on the propagation of the first longitudinal mode in the thin bar model, which yields $t_{\text{WR}} \approx \frac{2L}{c}$, where $L = 132'' - r$ is the distance between the strain gauge and the point where the bar's widening begins. This observation confirms that the partial reflection of the stress wave occurs at the area where the bar geometry begins to change (which leads to the associated change of the impedance). Note that the difference between the simulation results and the theoretical prediction slightly increases with r, which is likely due to the fact that the thin bar model approximation becomes less accurate as L decreases.

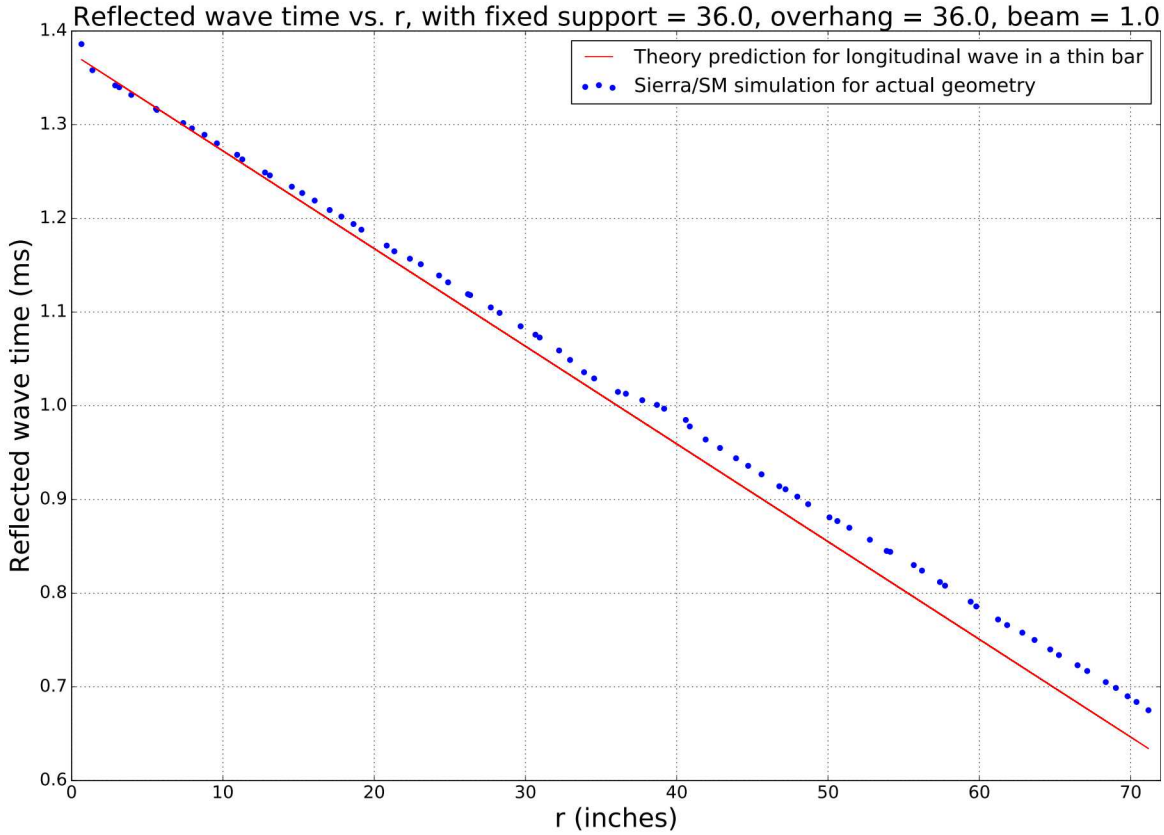

Figure 4-15. WRT versus r, for the SMD with $L_{\text{beam}} = 1''$, $L_{\text{supp}} = L_{\text{over}} = 36''$.

5. INVESTIGATION OF REFLECTED WAVE ENERGY

Based on results presented in section 4, extending the WRT is virtually impossible due to the fact that a partial reflection always occurs at the bar–beam boundary (or, for a monolithic design, at a point where the bar geometry changes). Instead, we decided to focus on minimizing the energy of the reflected wave, since a relatively weak reflected wave should not interfere much with the measurement of the stress–strain response.

5.1. Computation of the energy ratio

For this study, we decided to investigate the quantity $\mathcal{E}_R$, which is the ratio of energies between the reflected wave (from its start time to 10 ms) and the initial wave:

$$\mathcal{E}_R = \int_{t_{\mathrm{rws}}}^{t_{\mathrm{f}}} f^2(t)dt \Big/ \int_{t_{\mathrm{iws}}}^{t_{\mathrm{iwe}}} f^2(t)dt. \tag{2}$$

Here, f is the raw stress force at the gauge, t_{iws} and t_{iwe} are the start and end times of the initial wave, t_{rws} is the start time of the reflected wave, and $t_{\mathrm{f}} = 10$ ms is the final time. Threshold conditions for finding t_{iws}, t_{iwe}, and t_{rws} are

- t_{iws} is the first time when $|f_{\mathrm{filt}}| \geq 0.1$ lbf for $t < 0.5$ ms
- t_{iwe} is the last time when $|f_{\mathrm{filt}}| \geq 0.1$ lbf for $t < 0.5$ ms
- t_{rws} is the first time when $|f_{\mathrm{filt}}| \geq 0.5$ lbf for $t \geq 0.5$ ms

As defined above, f_{filt} is the filtered stress force, obtained from f by applying a 5th-order filter with a pass frequency of 10 kHz at data interpolated to a time step of 1.0e-8 s.

We evaluate the integrals in Eq. (2) by using the Simpson method (which is about 4% more accurate than simply summing over squared force values).

5.2. Comparing energy ratios for different bar–beam connections

Similarly to the analysis described in section 4.3, we investigated whether changing the bar–beam connection quality details affects the energy ratio. Specifically, we simulated the stress wave propagation over the time interval of 10 ms for 18 different connection variants (labeled from 0 to 17), shown in Table 4-1. In all these simulations, the wave beam geometry was fixed (see Figure 1-1) and the wave beam material was also fixed (AISI 4140).

Energy ratios obtained from the simulations for all 18 connection variants are reported in Table 5-1. We see that changing connection details can significantly affect the energy ratio. The smallest observed $\mathcal{E}_R$ value (1.557) is obtained for variant 9 (FTTFF) and the second smallest value (1.639) for variant 11 (FTFFF). The largest observed $\mathcal{E}_R$ values (from 4.223 to 4.286) are obtained for variants 12–15 (FFXXF). As described in section 4.3, T stands for "Tied" (welded or securely threaded) and F stands for "Frictional" (sliding), while X means that it can be either T or F. Variants 12–15 are the only ones for which all three connections to the bar (Bar/Nut Plate, Bar/Nut, and Bar/Beam) are frictional. In these configurations, nearly no load transfer would occur between the bar and the wave beam. This is confirmed by the very large $\mathcal{E}_R$ values for these variants, indicating that (almost) the entire stress wave is reflected down from the top end of the bar and (almost) none of it is transmitted to the wave beam to dissipate.

Table 5-1. Wave reflection times and energy ratios for AISI 4140 steel and 18 variants of the bar–beam connection.

Vari-ant	Bar / Nut Plate	Bar / Nut	Nut Plate / Nut	Nut Plate / Beam	Bar / Beam	t_{WR} (ms)	$\mathcal{E}_R$
0	tied	tied	tied	tied	frictional	1.360	2.160
1	tied	tied	tied	frictional	frictional	1.361	1.746
2	tied	tied	frictional	tied	frictional	1.361	2.091
3	tied	tied	frictional	frictional	frictional	1.361	1.864
4	tied	frictional	tied	tied	frictional	1.361	1.956
5	tied	frictional	tied	frictional	frictional	1.361	1.663
6	tied	frictional	frictional	tied	frictional	1.361	1.947
7	tied	frictional	frictional	frictional	frictional	1.361	1.786
8	frictional	tied	tied	tied	frictional	1.386	2.214
9	frictional	tied	tied	frictional	frictional	1.386	1.557
10	frictional	tied	frictional	tied	frictional	1.389	1.959
11	frictional	tied	frictional	frictional	frictional	1.389	1.639
12	frictional	frictional	tied	tied	frictional	1.371	4.223
13	frictional	frictional	tied	frictional	frictional	1.371	4.286
14	frictional	frictional	frictional	tied	frictional	1.371	4.260
15	frictional	frictional	frictional	frictional	frictional	1.371	4.252
16	frictional	frictional	frictional	frictional	tied	1.363	1.872
17	tied	tied	tied	tied	tied	1.356	2.176

Figure 5-1 shows the filtered force signal for three connection variants: 9 (FTTFF, $\mathcal{E}_R = 1.557$, the smallest energy ratio value), 0 (TTTTF, $\mathcal{E}_R = 2.160$, the variant implemented in the current experiment and the default one in the studies where the connection quality details are fixed), and 13 (FFTFF, $\mathcal{E}_R = 4.286$, the largest energy ratio value). Figure 5-1 clearly demonstrates that the amplitude of the reflected wave can be significantly influenced by the connection fixities. In particular, for variant 13, the amplitude of the reflected wave when it traverses the gauge for the first time is equal

to the amplitude of the initial wave, confirming that the entire stress wave is reflected down from the top of the bar when all connections to the bar are frictional.

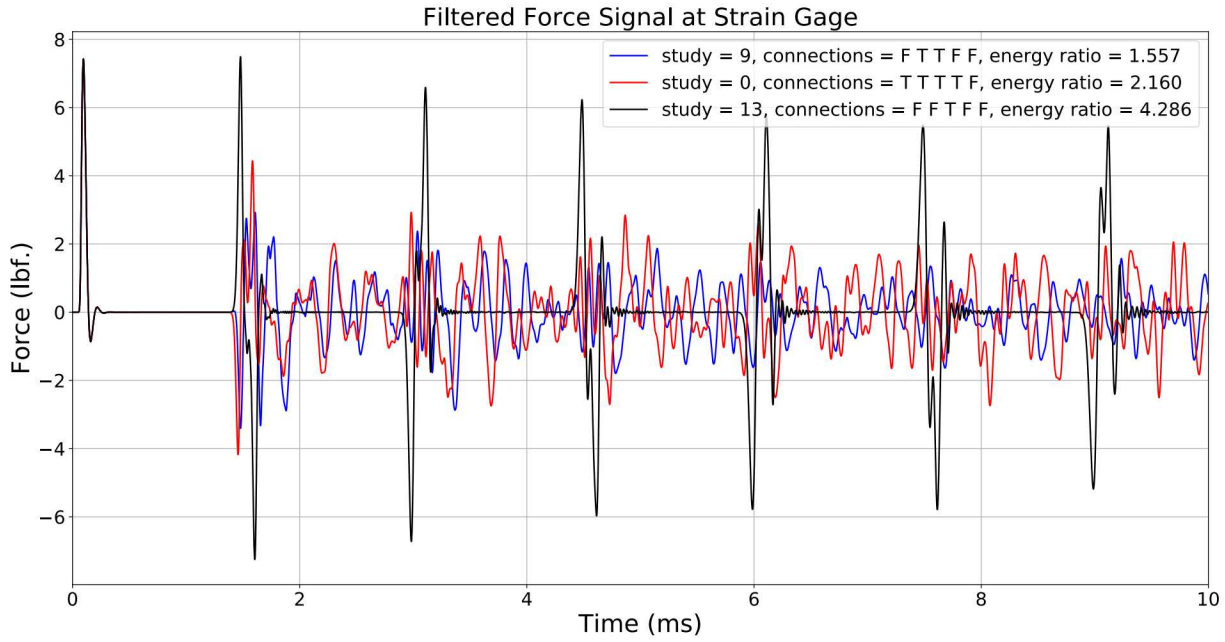

Figure 5-1. Simulated stress wave propagation (filtered force signal) over 10 ms, for three connection variants.

5.3. Comparing energy ratios for different wave beam materials

Similarly to the analysis described in section 4.4, we investigated whether changing the properties of the wave beam material affects the energy ratio (again, this analysis uses the wave beam material change as a proxy for the wave beam geometry change). Specifically, we simulated the stress wave propagation over the time interval of 10 ms for 660 hypothetical wave beam materials with varying values of the density ρ and Young's modulus E (up to two orders of magnitude larger or smaller than those of AISI 4140). Respective c_{factor} values ranged from 0.01 to 80. In all these simulations, the wave beam geometry was fixed (see Figure 1-1) and the bar–beam connection was also fixed (variant 0 in Table 4-1).

The resulting energy ratio values for each of the hypothetical materials are plotted against c_{factor} in Figure 5-2, where dots are color-coded by a range of Z_{factor} values. We see that $\mathcal{E}_R$ varies in a broad range, from approximately 0.935 to approximately 4.3, depending on the material properties. The energy ratio increases with c_{factor} as the latter grows from about 0.1 to 10, but stays in a relatively tight range (indicative of a saturation) for $c_{\text{factor}} < 0.1$ and $c_{\text{factor}} > 10$.

As seen from the color-coding in Figure 5-2, the spread between $\mathcal{E}_R$ values obtained for materials with the same value of c_{factor} can be explained by the difference in the respective values of Z_{factor}. To better understand the non-trivial dependence of the energy ratio on the impedance, we plot $\mathcal{E}_R$ against Z_{factor} in Figure 5-3, where dots are color-coded by a range of c_{factor} values. We find that best values of the energy ratio are obtained for Z_{factor} values in the range 0.5–0.8. Based on these results, we conclude that the key property of the wave beam material that determines the energy of the reflected wave is the sound velocity but the impedance also plays an important role.

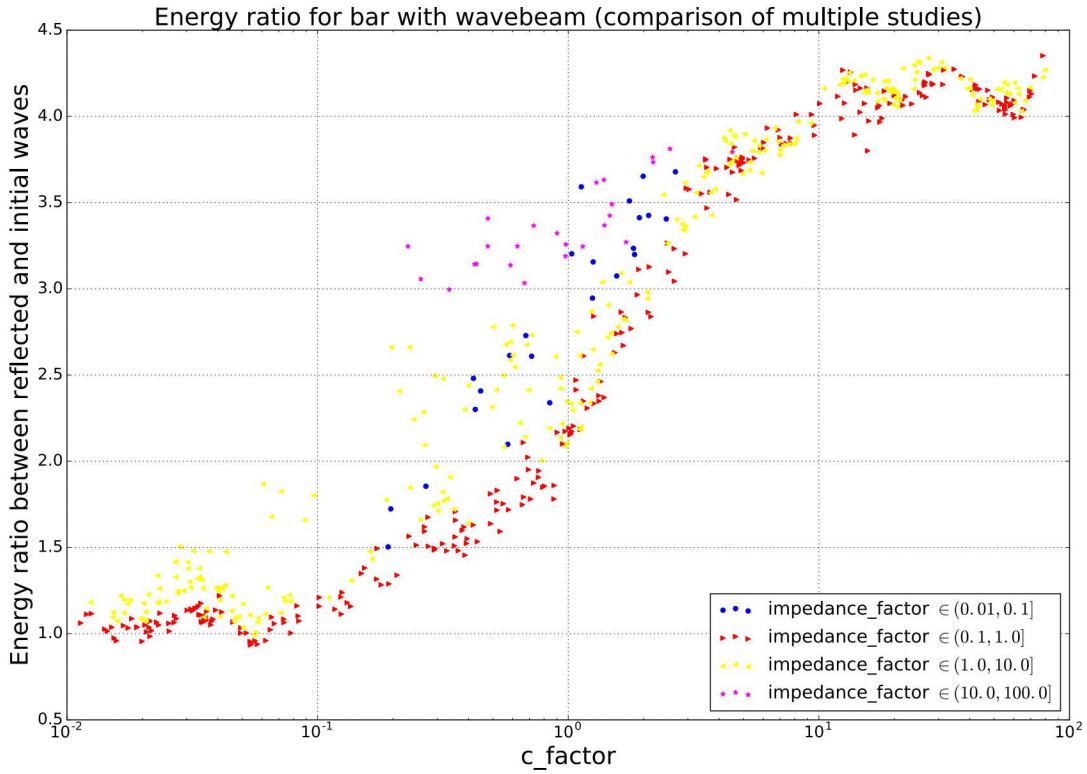

Figure 5-2. Energy ratio $\mathcal{E}_R$ versus $c_{\mathbf{factor}}$ for 660 hypothetical wave beam materials, color-coded by a range of $Z_{\mathbf{factor}}$ values.

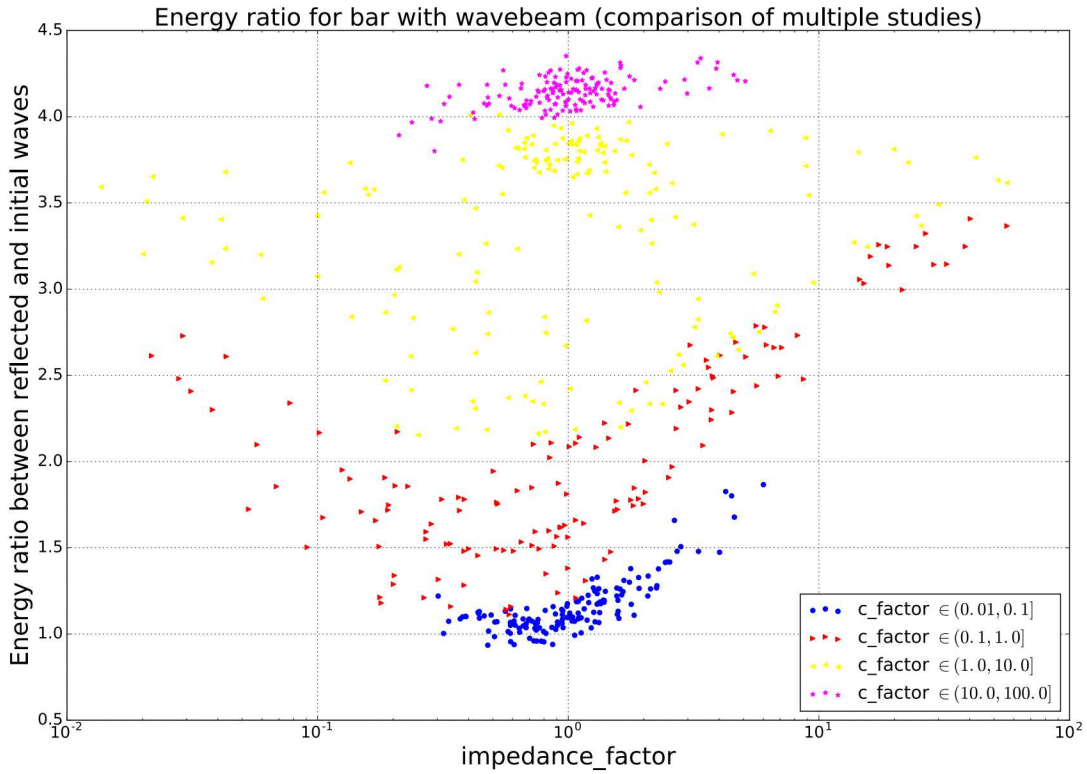

Figure 5-3. Energy ratio $\mathcal{E}_R$ versus $Z_{\mathbf{factor}}$ for 660 hypothetical wave beam materials, color-coded by a range of $c_{\mathbf{factor}}$ values.

Examples of three typical filtered force signals for hypothetical materials with small, medium, and large values of c_{factor} are shown in Figure 5-4. We see that the reflected wave amplitude can be significantly decreased by choosing a wave beam material with optimal c_{factor} and Z_{factor} values. Also, as the reflected wave travels up and down the bar, it traverses through the gauge six times over 10 ms. This observation explains why the energy ratio values shown in Figure 5-2 and Figure 5-3 are relatively large (and in many cases larger than one), even so only a small portion of the stress wave is reflected from the bar–beam boundary.

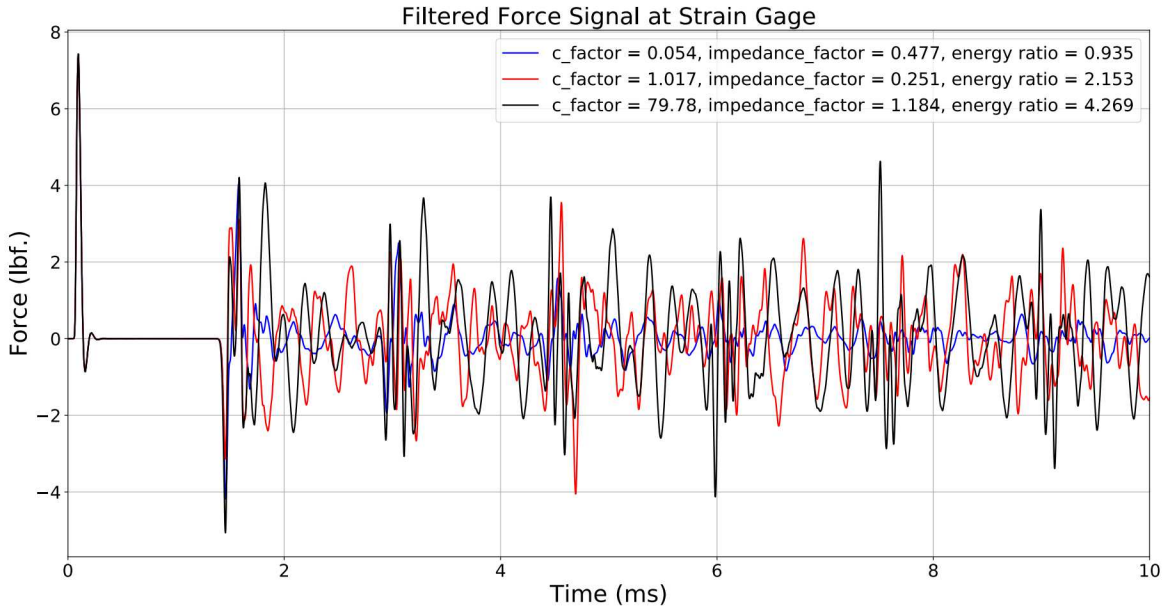

Figure 5-4. Simulated stress wave propagation (filtered force signal) over 10 ms, for three hypothetical wave beam materials.

5.4. Varying both the bar–beam connection and the wave beam material

We also investigated how the energy ratio is influenced when we vary both the bar–beam connection quality details and the wave beam material. In simulations performed for this investigation, the wave beam geometry was fixed (see Figure 1-1).

First, we studied how different connection variants perform for a particular hypothetical wave beam material (that we refer to as Material X), which results in the smallest $\mathcal{E}_R$ value (0.935) for connection variant 0. Properties of Material X are described in Table 5-2. The filtered force signal for Material X and connection variant 0 is shown by the blue line in Figure 5-4.

Table 5-2. Properties of Material X and Material Y.

Material	$\log_{10}\left(\frac{\rho}{\rho_{4140}}\right)$	$\log_{10}\left(\frac{E}{E_{4140}}\right)$	$c_{\text{factor}} = \frac{c}{c_{4140}}$	$Z_{\text{factor}} = \frac{Z}{Z_{4140}}$
X	0.946550978	−1.588835443	0.05398919	0.47737291
Y	1.215100035	−1.196544067	0.06225553	1.02159318

We simulated the stress wave propagation over the time interval of 10 ms for Material X and all 18 connection variants. The resulting energy ratios are reported in Table 5-3. We see that when AISI

4140 is replaced by Material X, energy ratio values decrease for most connection variants, with a notable exception of variants 12–15, for which $\mathcal{E}_R$ values still remain very large (> 4.2). This observation confirms our conclusion that in cases where all three connections to the bar are frictional, the presence of the wave beam plays no role due to the complete reflection of the stress wave from the top of the bar. On the other hand, we see very significant improvements for connection variants 17 (TTTTT, $\mathcal{E}_R$ decreases from 2.176 to 0.773) and 4 (TFTTF, $\mathcal{E}_R$ decreases from 1.956 to 0.821). We also see an improvement for connection variant 9, which achieves the smallest $\mathcal{E}_R$ value of 1.557 for AISI 4140, but the respective $\mathcal{E}_R$ value of 0.958 for Material X is only the seventh smallest among the 18 variants.

Table 5-3. Energy ratios for Material X and 18 variants of the bar–beam connection

Variant	Bar / Nut Plate	Bar / Nut	Nut Plate / Nut	Nut Plate / Beam	Bar / Beam	$\mathcal{E}_R$ for AISI 4140	$\mathcal{E}_R$ for Material X
0	tied	tied	tied	tied	frictional	2.160	0.935
1	tied	tied	tied	frictional	frictional	1.746	1.125
2	tied	tied	frictional	tied	frictional	2.091	0.985
3	tied	tied	frictional	frictional	frictional	1.864	1.146
4	tied	frictional	tied	tied	frictional	1.956	0.821
5	tied	frictional	tied	frictional	frictional	1.663	0.970
6	tied	frictional	frictional	tied	frictional	1.947	0.949
7	tied	frictional	frictional	frictional	frictional	1.786	1.125
8	frictional	tied	tied	tied	frictional	2.214	0.864
9	frictional	tied	tied	frictional	frictional	1.557	0.958
10	frictional	tied	frictional	tied	frictional	1.959	0.984
11	frictional	tied	frictional	frictional	frictional	1.639	0.947
12	frictional	frictional	tied	tied	frictional	4.223	4.219
13	frictional	frictional	tied	frictional	frictional	4.286	4.258
14	frictional	frictional	frictional	tied	frictional	4.260	4.253
15	frictional	frictional	frictional	frictional	frictional	4.252	4.259
16	frictional	frictional	frictional	frictional	tied	1.872	1.857
17	tied	tied	tied	tied	tied	2.176	0.773

Next, we investigated how connection variants with lowest energy ratios perform over a range of hypothetical wave beam materials. In addition to connection variant 0 (TTTTF), whose performance with respect to different wave beam materials is described in section 5.3, we considered three more variants: 9 (FTTFF, smallest $\mathcal{E}_R$ value for AISI 4140), 17 (TTTTT, smallest $\mathcal{E}_R$ value for Material X), and 4 (TFTTF, second smallest $\mathcal{E}_R$ value for Material X). Specifically, for each of these three variants, we performed simulations for 300 hypothetical wave beam materials with varying values of the density ρ (up to two orders of magnitude larger than that of AISI 4140) and Young's modulus E (up to two orders of magnitude smaller than that of AISI 4140).

Figure 5-5 shows the resulting energy ratios plotted against c_{factor} (with $c_{\text{factor}} \in [0.01, 1.0]$), where dots are color-coded by the connection variant. We observe that for hypothetical materials with $0.25 \lesssim c_{\text{factor}} \lesssim 1.0$ (i.e., with properties relatively close to those of AISI 4140), $\mathcal{E}_R$ values are smallest for connection variant 9. For hypothetical materials with $c_{\text{factor}} \lesssim 0.25$, $\mathcal{E}_R$ values are smallest for connection variant 17. The improvement in energy ratio saturates for $c_{\text{factor}} \lesssim 0.08$. The best overall $\mathcal{E}_R$ value we found in this investigation is 0.707, obtained for connection variant 17 and a hypothetical material that we refer to as Material Y. Properties of Material Y are described in Table 5-2.

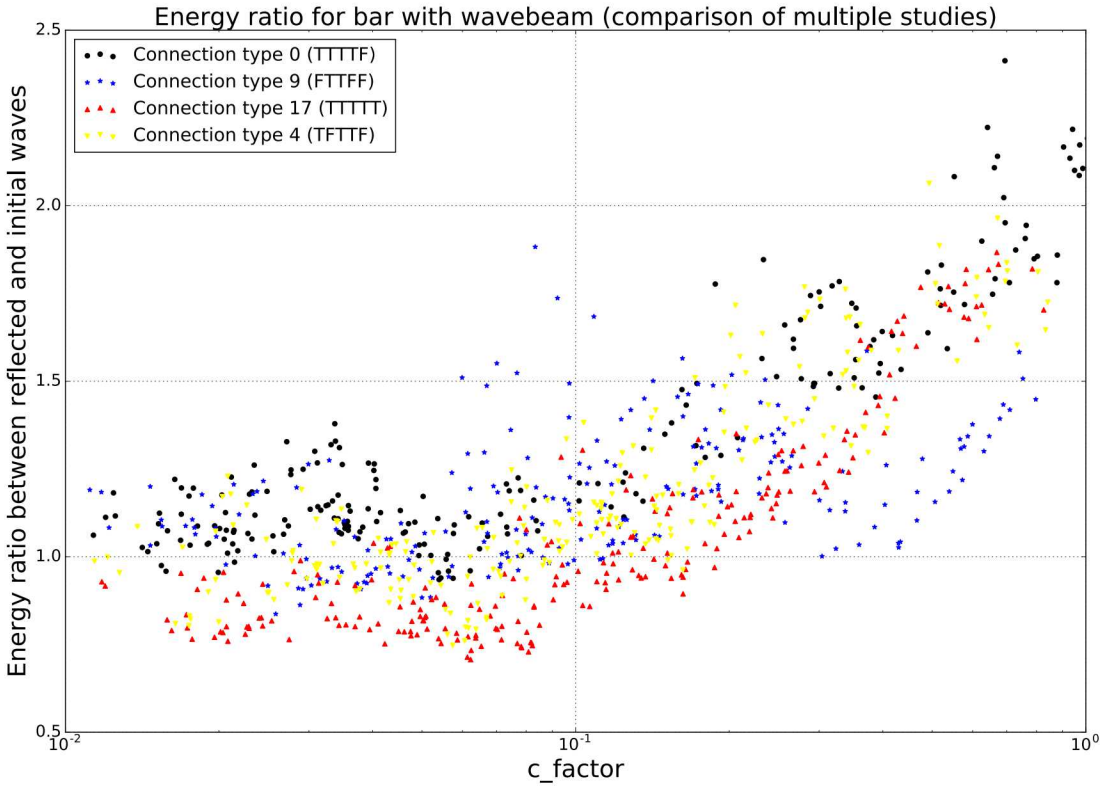

Figure 5-5. Energy ratio $\mathcal{E}_R$ versus c_{factor} for connection variants 0, 9, 17, 4 and various hypothetical wave beam materials.

Figure 5-6 shows filtered force signals for the cases of connection variant 0 with Material X (the blue line, the same as the blue line in Figure 5-4) and connection variant 17 with Material Y (the red line). As said above, Material X results in the smallest $\mathcal{E}_R$ value (0.935) for variant 0, and Material Y results in the smallest $\mathcal{E}_R$ value (0.707) for variant 17 and, furthermore, among all combinations of connection variants and hypothetical wave beam materials that we studied.

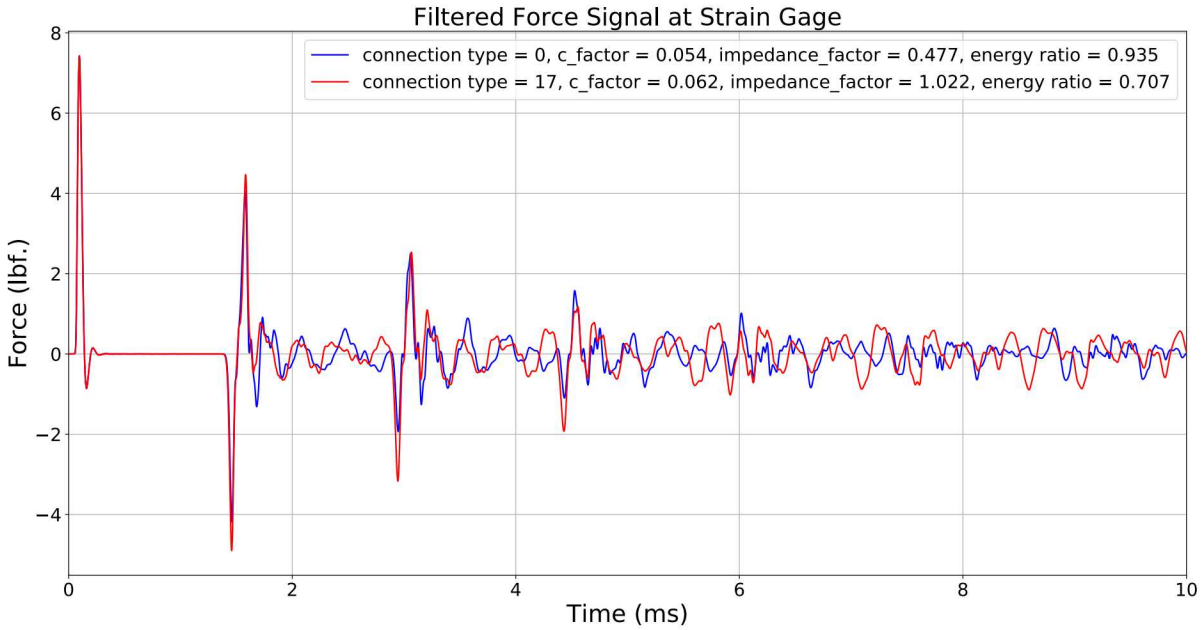

Figure 5-6. Simulated stress wave propagation (filtered force signal) over 10 ms, for connection variant 0 with Material X and connection variant 17 with Material Y.

5.5. Asymmetric monolithic design of the Dropkinson bar

Finally, we investigated whether it is possible to significantly reduce the energy of the reflected wave by using a monolithic design of the bar-and-beam system. In this investigation we consider a modification to the SMD described in section 4.5. Specifically, we propose an asymmetric monolithic design (AMD), which is shown in Figure 5-7 and whose parameters are described in Table 5-4. We assume that the monolithic bar-and-beam system is made of Maraging C300 steel.

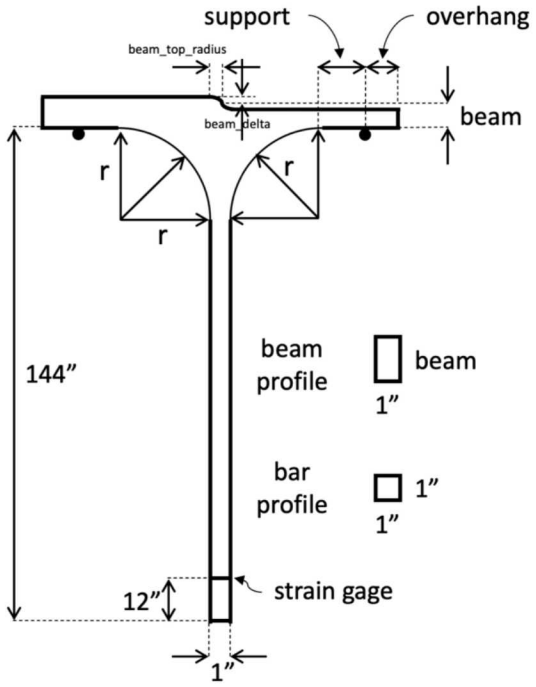

Figure 5-7. Asymmetric monolithic design (AMD) of the bar-and-beam system.

Table 5-4. Parameters of the asymmetric monolithic design (AMD) of the bar-and-beam system.

Parameter	Notation	Description
r	$\boldsymbol{r}$	radius of bar curvature
beam	$\boldsymbol{L_{\mathrm{beam}}}$	average beam thickness
support	$\boldsymbol{L_{\mathrm{supp}}}$	distance from r to support
overhang	$\boldsymbol{L_{\mathrm{over}}}$	distance past support
beam delta	$\boldsymbol{\Delta_{\mathrm{beam}}}$	difference in beam thickness between right and left halves
beam left	$\boldsymbol{L_{\mathrm{bl}} = L_{\mathrm{beam}} - 0.5\Delta_{\mathrm{beam}}}$	thickness of beam's left half
beam right	$\boldsymbol{L_{\mathrm{br}} = L_{\mathrm{beam}} + 0.5\Delta_{\mathrm{beam}}}$	thickness of beam's right half
beam top radius (BTR)	r_{btop}	radius of curvature for connection between beam's left and right halves

Figure 5-8 shows two views of the AMD model geometry for a specific combination of parameter values: $r = 19.1''$, $L_{\mathrm{beam}} = r = 19.1''$, $L_{\mathrm{supp}} = 32.178''$, $L_{\mathrm{over}} = 85'' - L_{\mathrm{supp}} = 52.822''$, $\Delta_{\mathrm{beam}} = 0.94\, r = 17.954''$, $r_{\mathrm{btop}} = 10''$. As will be shown in section 5.5.5, the AMD with these parameter values results in a very small energy ratio value: $\mathcal{E}_R = 0.451$.

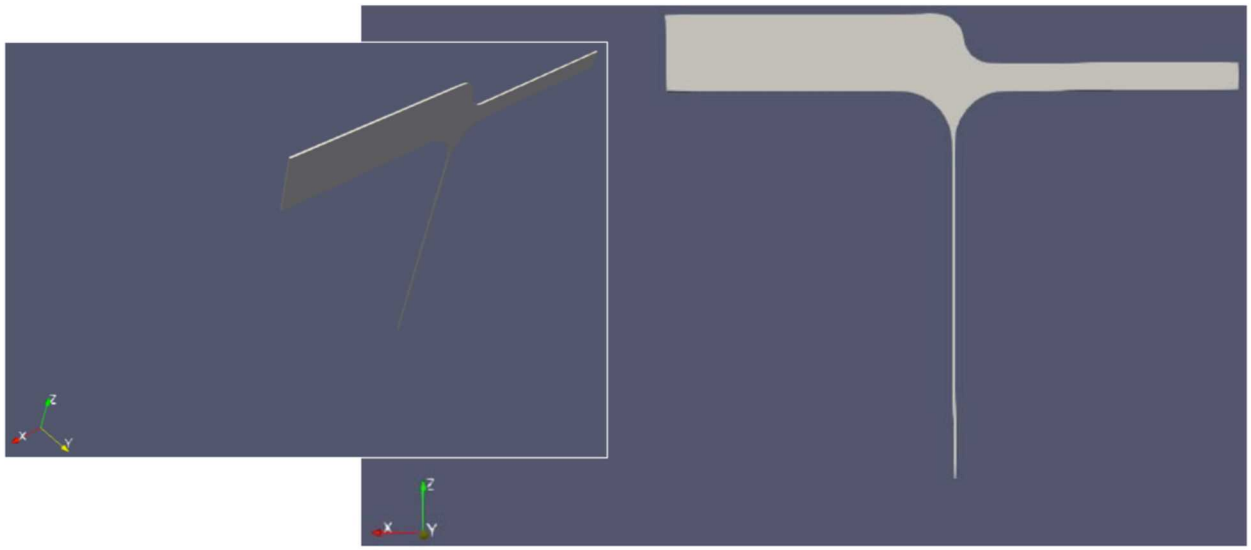

Figure 5-8. Views of the AMD model geometry.

As seen from Figure 5-7 and Figure 5-8, the difference between SMD and AMD is that in the latter case the beam's left and right halves have a different thickness. This design was inspired by the observation that the sign of the reflected wave's amplitude can depend on the beam thickness (cf. Figure 4-9). Therefore, the motivation for the AMD is to create a destructive interference between the waves reflected down from the left and right parts of the top surface of the beam, thus directing a significant portion of the reflected wave towards the arms of the beam where it is more likely to dissipate.

5.5.1. Dependence of energy ratio on beam delta

We investigated the dependence of the energy ratio on various AMD parameters. First, we performed simulations in which we varied the value of Δ_{beam} in the range from $0''$ to $1''$. In one set of simulations, we also varied the value of the beam top radius (BTR) to keep $r_{\mathrm{btop}} = \Delta_{\mathrm{beam}}$, while values of the other parameter were fixed: $r = 1''$, $L_{\mathrm{beam}} = 1''$, $L_{\mathrm{supp}} = 15''$, $L_{\mathrm{over}} = 44''$. The resulting energy ratios (blue dots) and WRTs (red dots) are plotted against Δ_{beam} in Figure 5-9. We see that the energy ratio oscillates as a function of Δ_{beam} and has the global minimum at $\Delta_{\mathrm{beam}} \approx 0.94''$.

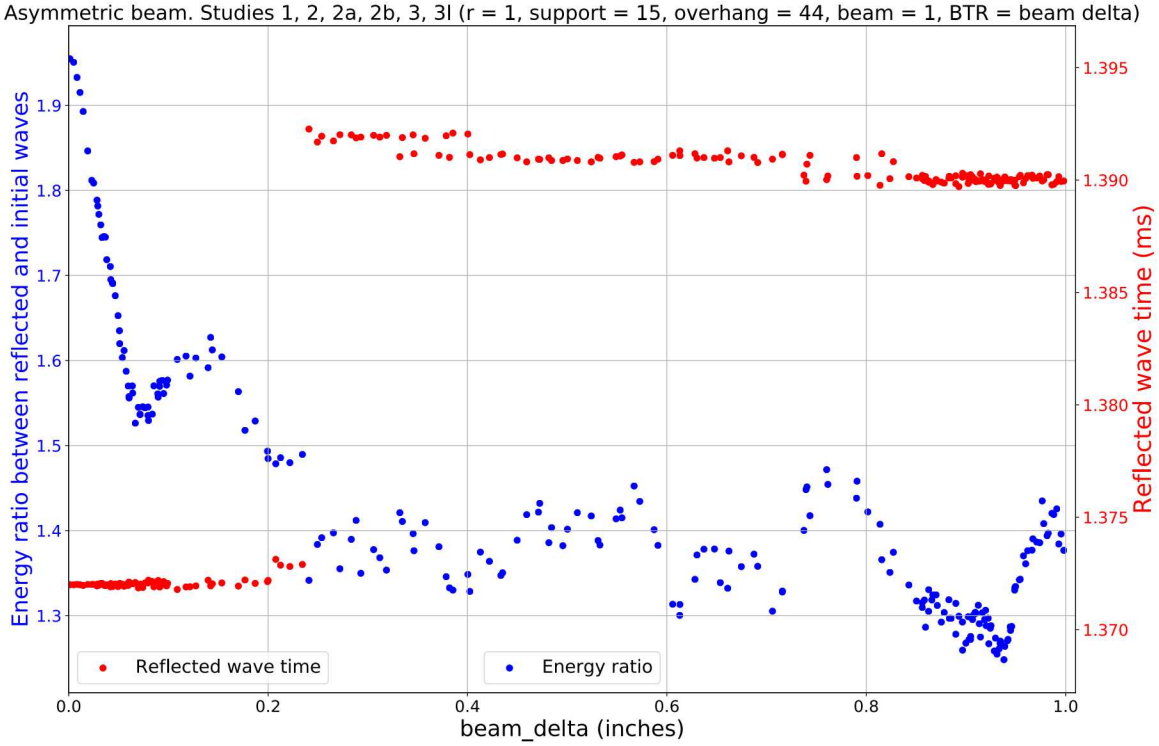

Figure 5-9. Energy ratio $\mathcal{E}_R$ and WRT t_{WR} versus Δ_{beam} for AMD with $r_{\mathrm{btop}} = \Delta_{\mathrm{beam}}$ and fixed values of other parameters.

We also performed additional sets of simulations with Δ_{beam} varying in the range from $0''$ to $1''$ and different fixed r_{btop} values ($0.5''$, $1''$, $10''$, $25''$, $50''$), while the other parameters had the same fixed values as described above. The energy ratios obtained for all these sets of simulations are plotted against Δ_{beam} in Figure 5-10, where dots are color-coded by the r_{btop} value. We once again see an oscillating pattern for $\mathcal{E}_R$ as a function of Δ_{beam}, and the global minimum is still near the same value of $\Delta_{\mathrm{beam}} \approx 0.94''$. The smallest values of $\mathcal{E}_R$ are obtained for $r_{\mathrm{btop}} = 10''$.

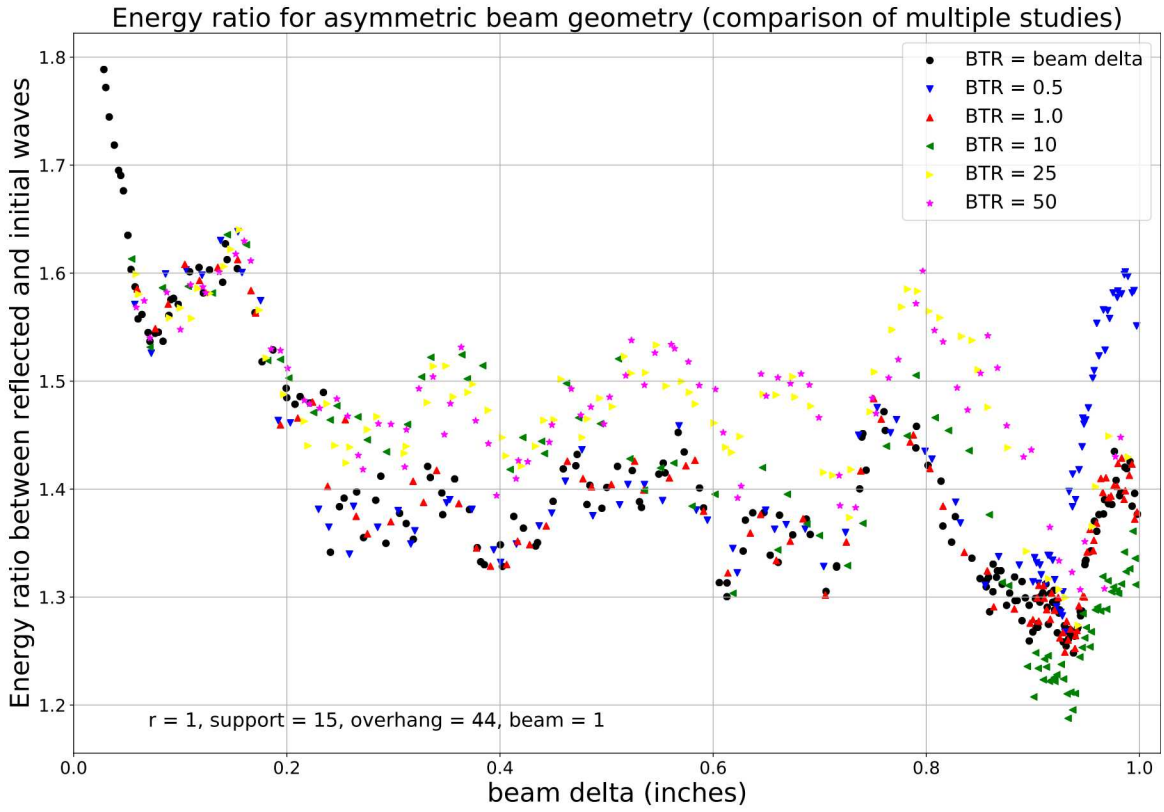

Figure 5-10. Energy ratio $\mathcal{E}_R$ versus Δ_{beam} for AMD with various values of r_{btop} and fixed values of other parameters.

5.5.2. Dependence of energy ratio on radius of bar curvature

Next, we performed simulations in which we varied the value of r while keeping $r_{\text{btop}} = 10''$ fixed. For the rest of AMD parameters, we considered four combinations of values:

(a) $L_{\text{beam}} = 1''$, $L_{\text{supp}} = 16'' - r$, $L_{\text{over}} = 44''$, $\Delta_{\text{beam}} = 0.94''$

(b) $L_{\text{beam}} = 1''$, $L_{\text{supp}} = 15''$, $L_{\text{over}} = 44''$, $\Delta_{\text{beam}} = 0.94''$

(c) $L_{\text{beam}} = r$, $L_{\text{supp}} = 16'' - r$, $L_{\text{over}} = 44''$, $\Delta_{\text{beam}} = 0.94\, r$

(d) $L_{\text{beam}} = r$, $L_{\text{supp}} = 15''$, $L_{\text{over}} = 44''$, $\Delta_{\text{beam}} = 0.94\, r$

The energy ratios obtained for all these simulations are plotted against r in Figure 5-11, where dots are color-coded by the combination of parameter values (black for combination (a), blue for combination (b), red for combination (c), and yellow for combination (d)). We see that the pair of combinations (a) and (b), where L_{beam} and Δ_{beam} have fixed values ($L_{\text{beam}} = 1''$ and $\Delta_{\text{beam}} = 0.94''$) perform best for small r values ($r < 1''$). On the other hand, the pair of combinations (c) and (d), where L_{beam} and Δ_{beam} increase linearly with r ($L_{\text{beam}} = r$ and $\Delta_{\text{beam}} = 0.94\, r$) perform best for large r values. The WRTs obtained for the same four combinations of parameter values are plotted against r in Figure 5-12. We see a familiar dependence of t_{WR} on r (cf. Figure 4-15), with a "jump" in the WRT value at $r = 1''$. Note that the WRT trends for the pair of combinations with $L_{\text{beam}} = 1''$ and the pair of combinations with $L_{\text{beam}} = r$ differ only for $r < 1''$.

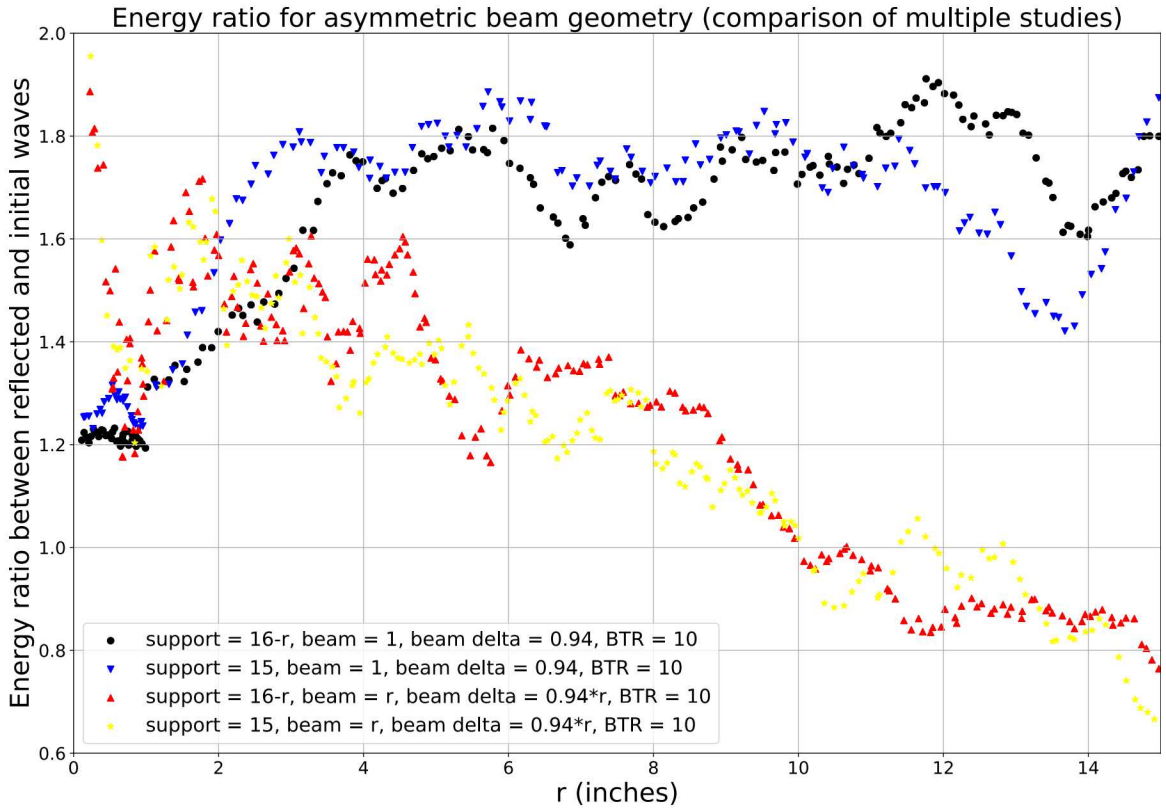

Figure 5-11. Energy ratio $\mathcal{E}_R$ versus r for AMD with four parameter value combinations.

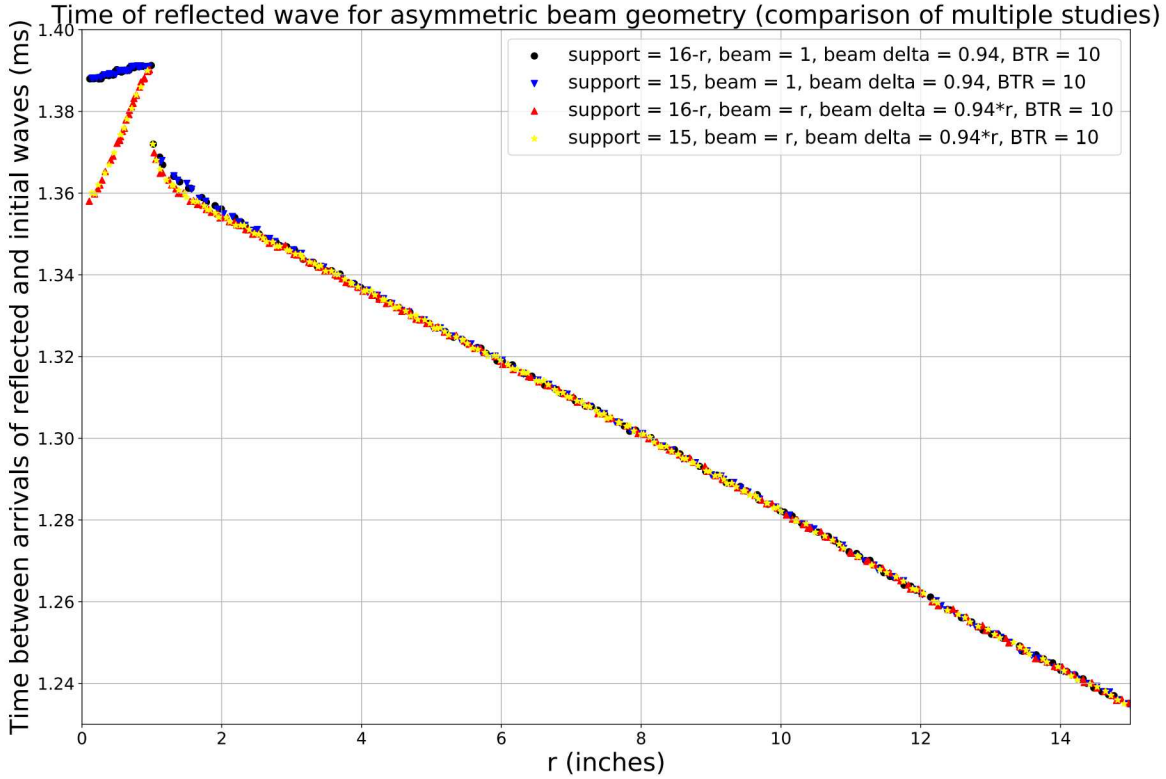

Figure 5-12. WRT t_{WR} versus r for AMD with four parameter value combinations.

We took a closer look at combination (d) that appears to result in the best performance (in terms of minimizing the energy ratio) for $r \gg 1''$. The resulting energy ratios (blue dots) and WRTs (red dots) are plotted against r in Figure 5-13. The overall trend for $\mathcal{E}_R$ is to improve (i.e., decrease) as r increases, but it also exhibits oscillations that result in multiple local minima at various values of r. To maintain reasonable parameter values with respect to manufacturing capabilities, we restricted our investigation to $r < 20''$. Therefore, we will focus our attention on local minima at $r \approx 15.1''$ and $r \approx 19.1''$.

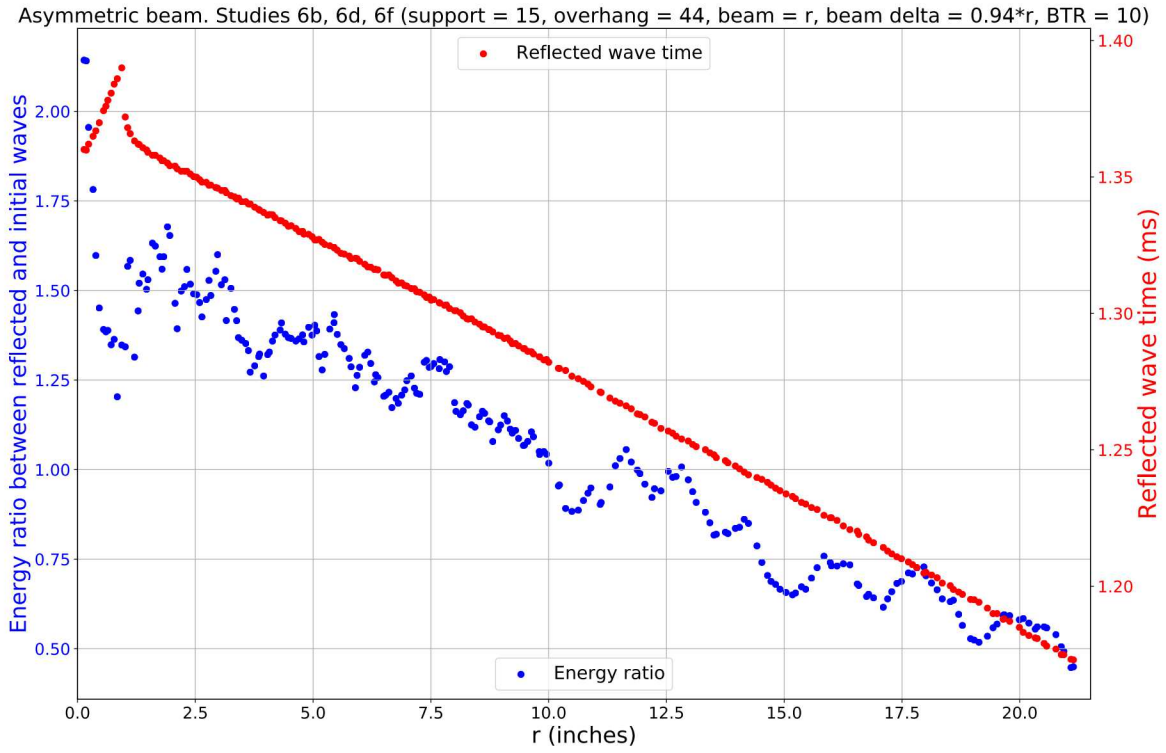

Figure 5-13. Energy ratio $\mathcal{E}_R$ and WRT t_{WR} versus r for AMD with $r_{\mathrm{btop}} = 10''$ and combination (d) of other parameter values.

5.5.3. Dependence of energy ratio on beam top radius

From the analysis described in in section 5.5.1, we found that the BTR value of $r_{\mathrm{btop}} \approx 10''$ is optimal when $r = L_{\mathrm{beam}} = 1''$. However, what is the optimal value of r_{btop} when r and $L_{\mathrm{beam}} = r$ are larger, in particular, for the local minima at $r \approx 15.1''$ and $r \approx 19.1''$? To answer this question, we performed simulations with r_{btop} varying between $0.5''$ and $50''$. Figure 5-14 shows the resulting energy ratios (blue dots) and WRTs (red dots), plotted against r_{btop}, for $r = 19.1''$ and combination (d) of other parameter values. We see that, for these parameter values, the energy ratio has a sharp minimum at $r_{\mathrm{btop}} \approx 10''$. Figure 5-15 shows the resulting energy ratios, plotted against r_{btop}, for three different values of r ($r = 1''$, $r = 15.1''$, and $r = 19.1''$) and combination (d) of other parameter values. In the cases $r = 1''$ and $r = 15.1''$, the energy ratio does not have a sharp minimum at $r_{\mathrm{btop}} \approx 10''$ but its value at $r_{\mathrm{btop}} = 10''$ is still reasonably small (compared to other $\mathcal{E}_R$ values in the set with the same value of r).

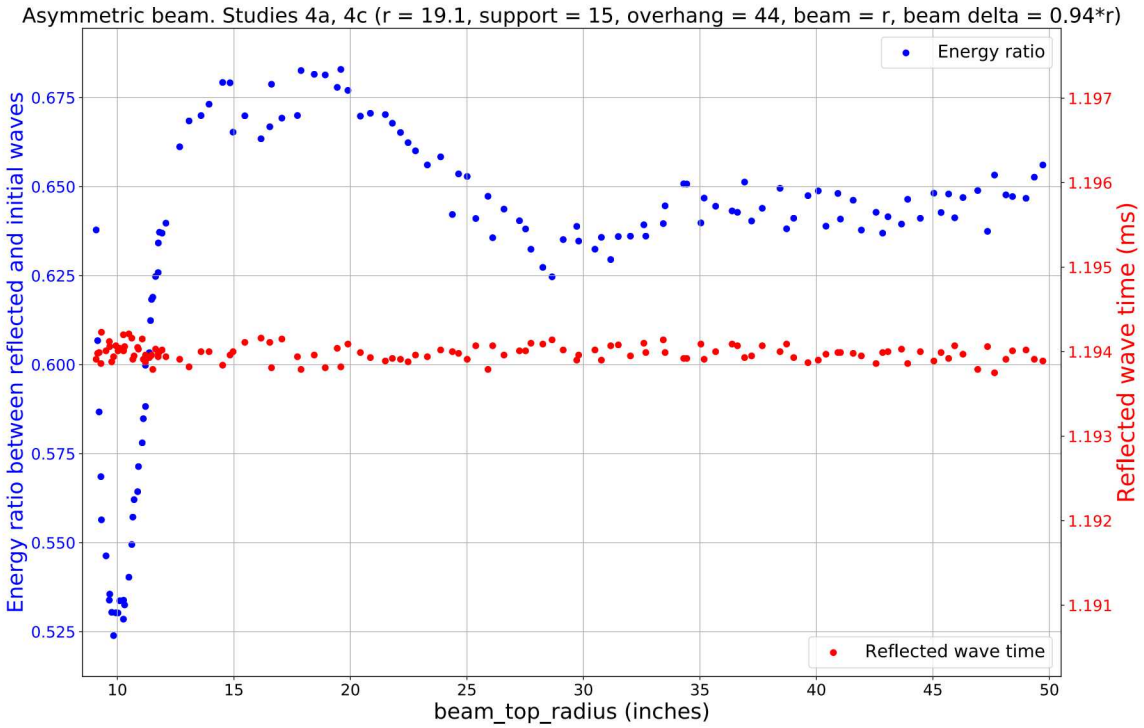

Figure 5-14. Energy ratio $\mathcal{E}_R$ and WRT t_{WR} versus r_{btop} for AMD with $r = 19.1''$ and combination (d) of other parameter values.

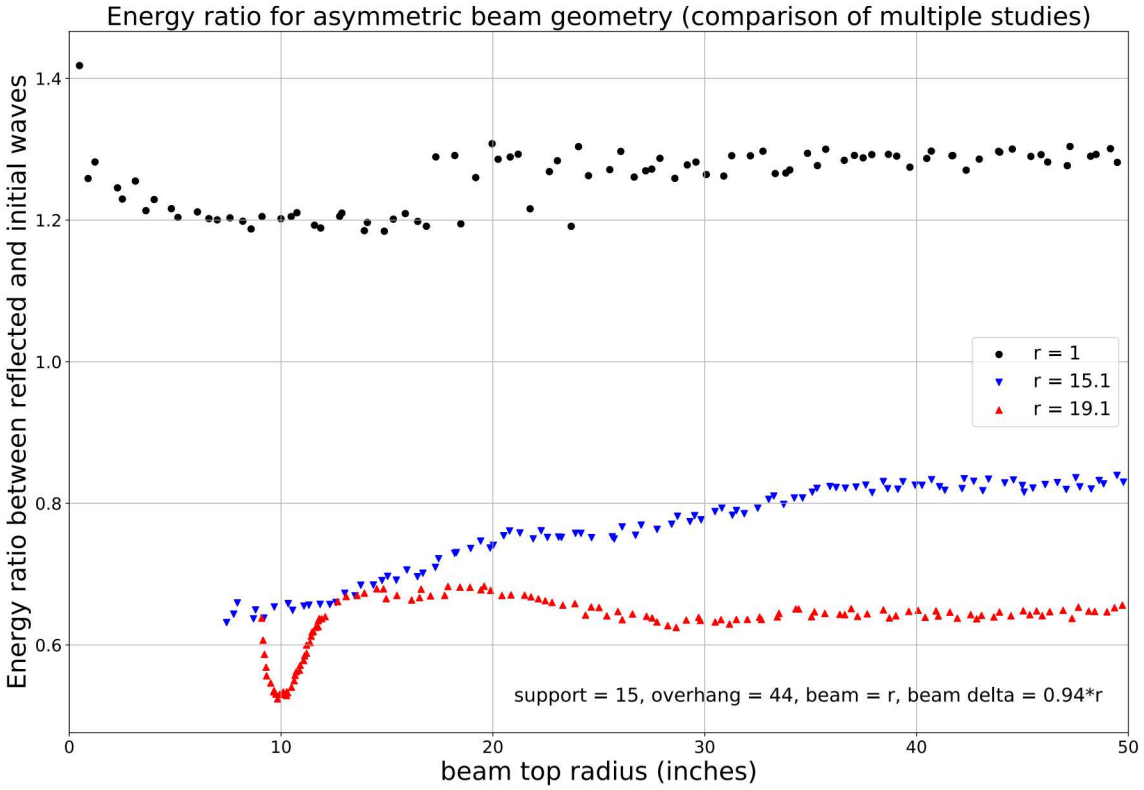

Figure 5-15. Energy ratio $\mathcal{E}_R$ versus r_{btop} for AMD with three different values of r and combination (d) of other parameter values.

5.5.4. Dependence of energy ratio on beam delta and average beam thickness for optimal value of radius of bar curvature

Based on the analysis in section 5.5.2 and section 5.5.3, we decided to use the parameter values $r = 19.1''$ and $r_{\text{btop}} = 10''$ in order to minimize the energy ratio. Next, we want to verify that the choices $\Delta_{\text{beam}} = 0.94\, r$ and $L_{\text{beam}} = r$ are optimal for $r = 19.1''$. We set $r = 19.1''$, $r_{\text{btop}} = 10''$, $L_{\text{supp}} = 15''$, $L_{\text{over}} = 44''$, and performed two additional sets of simulations.

In one set of simulations, we used $L_{\text{beam}} = r = 19.1''$ and varied the ratio $\frac{\Delta_{\text{beam}}}{r}$ between 0.1 and 1.0. The resulting energy ratios (blue dots) and WRTs (red dots) are plotted against $\frac{\Delta_{\text{beam}}}{r}$ in Figure 5-16. These results confirm that the choice $\Delta_{\text{beam}} = 0.94\, r$ is indeed optimal for $r = 19.1''$.

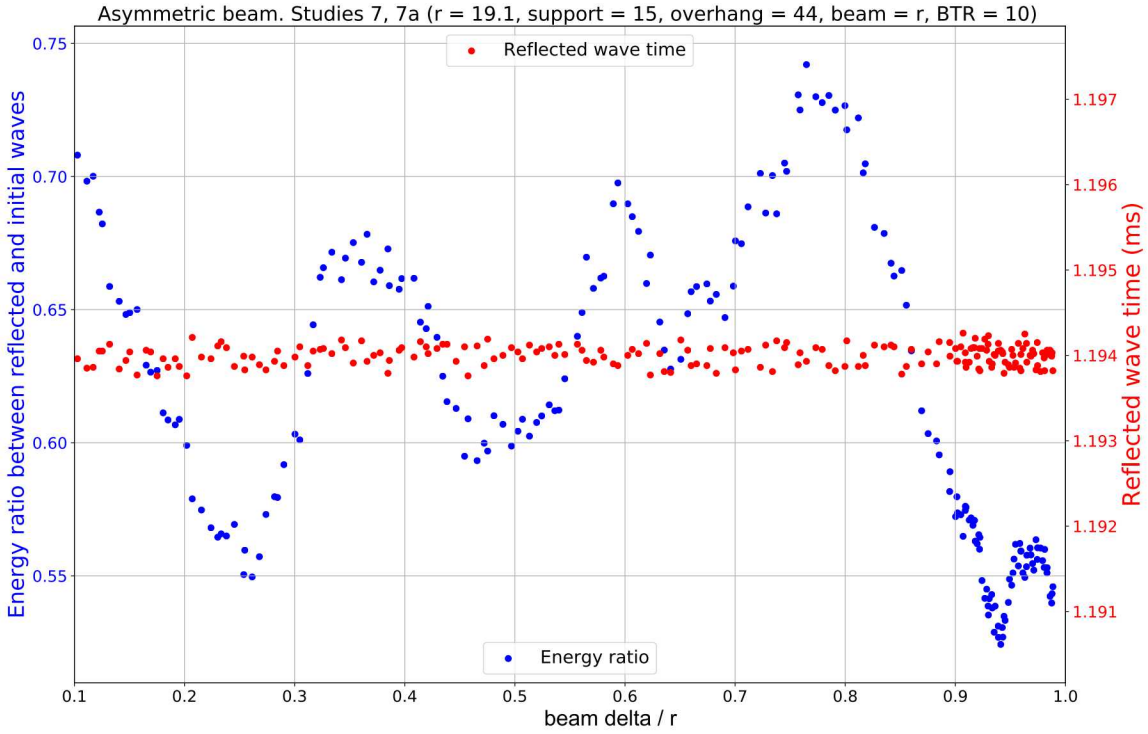

Figure 5-16. Energy ratio $\mathcal{E}_R$ and WRT t_{WR} versus the ratio Δ_{beam}/r for AMD with $r = 19.1''$ and $r_{\text{btop}} = 10''$.

In another set of simulations, we used $\Delta_{\text{beam}} = 0.94\, r$ and varied the value of L_{beam} between $8''$ and $30''$. The resulting energy ratios (blue dots) and WRTs (red dots) are plotted against L_{beam} in Figure 5-17. The energy ratio indeed has a local optimum at $L_{\text{beam}} \approx 19.1''$ (i.e., at the value equal to r). There also exist slightly better local minima at larger L_{beam} values, but they correspond to a beam which would be too thick for practical purposes.

We also performed the same type of analysis for $r = 15.1''$. The resulting energy ratios (blue dots) and WRTs (red dots) are plotted against L_{beam} in Figure 5-18. We see that the energy ratio has multiple local minima at various values of L_{beam}, including the one at $L_{\text{beam}} \approx 15.1''$ (i.e., at the value equal to r). However, the result obtained for $r = L_{\text{beam}} = 19.1''$ is more appealing.

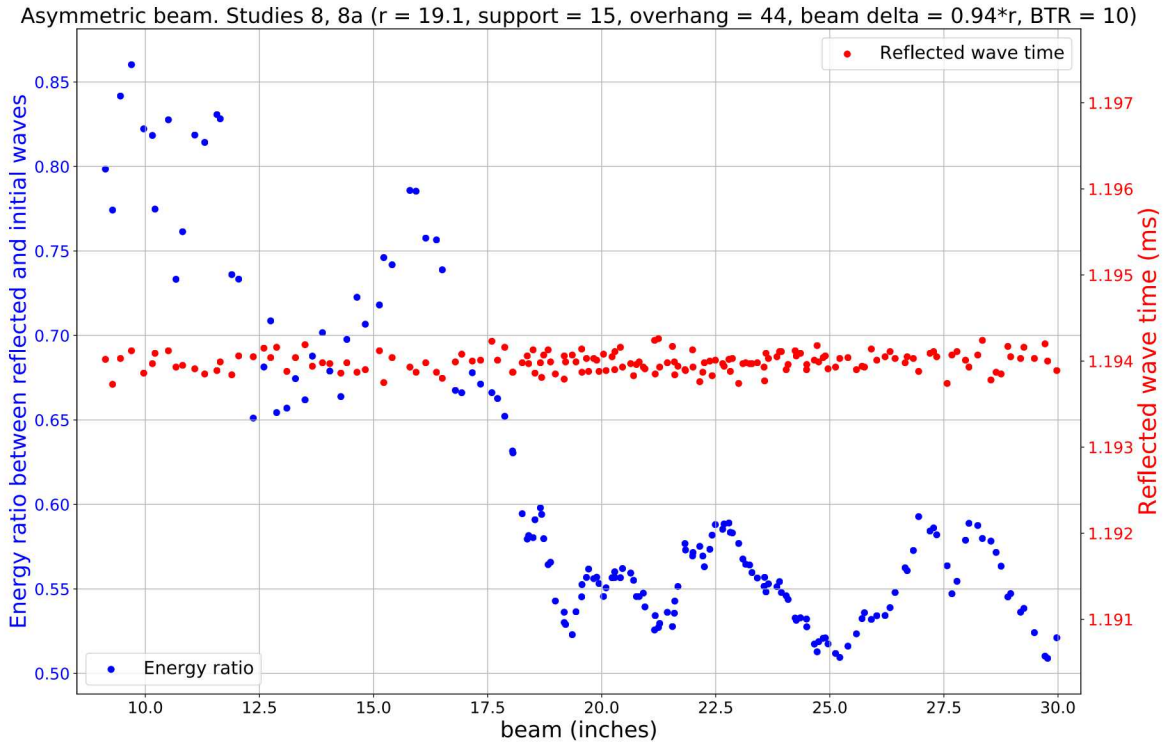

Figure 5-17. Energy ratio $\mathcal{E}_R$ and WRT t_{WR} versus $L_{\mathbf{beam}}$ for AMD with $r = 19.1''$ and $r_{\mathrm{btop}} = 10''$.

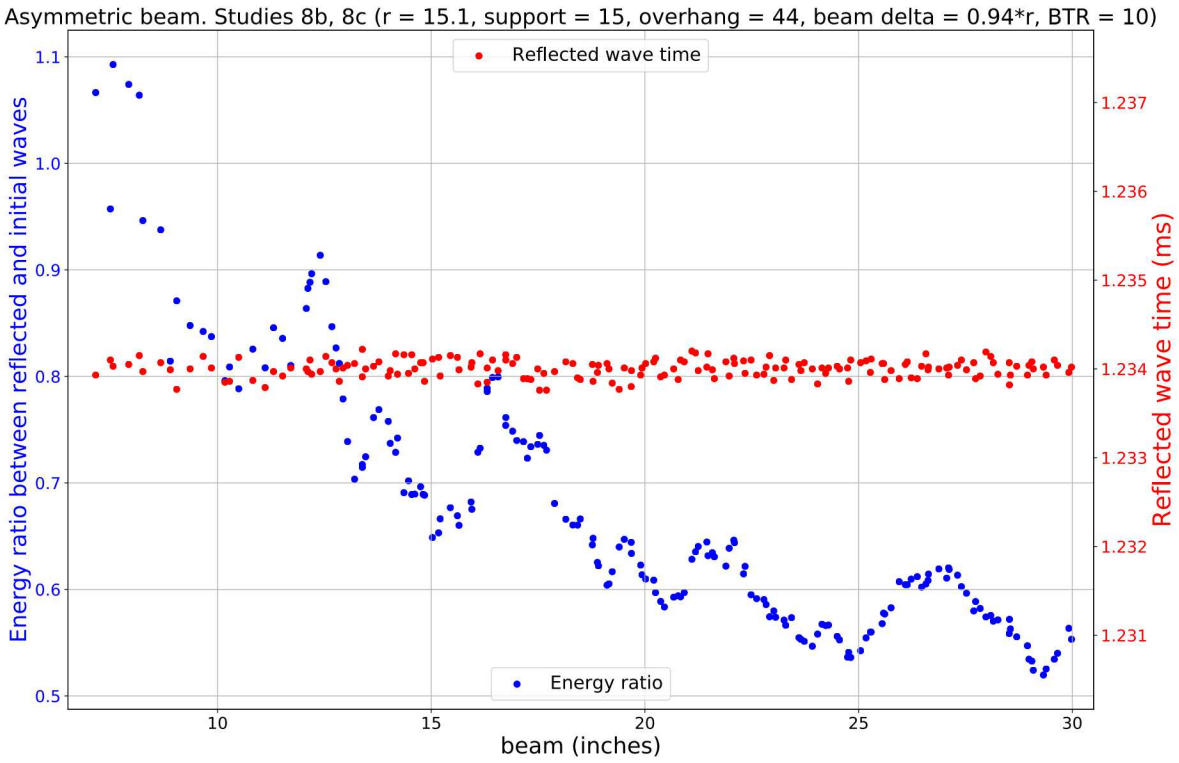

Figure 5-18. Energy ratio $\mathcal{E}_R$ and WRT t_{WR} versus $L_{\mathbf{beam}}$ for AMD with $r = 15.1''$ and $r_{\mathrm{btop}} = 10''$.

5.5.5. *Dependence of energy ratio on beam length*

The total length of the beam in the monolithic design is $2(r + L_{\text{supp}} + L_{\text{over}}) + 1''$. In previous analyses, we used the fixed values $L_{\text{supp}} = 15''$ and $L_{\text{over}} = 44''$. To investigate the dependence of the energy ratio on L_{supp} and on the total beam length, we performed four sets of simulations, in each of which we varied L_{supp} between $5''$ and $50''$ while keeping the value of $L_{\text{supp}} + L_{\text{over}}$ fixed. The values of $L_{\text{supp}} + L_{\text{over}}$ in these four sets of simulations were $59''$, $72''$, $85''$, and $98''$. Values of the other parameters were fixed: $r = 19.1''$, $L_{\text{beam}} = r = 19.1''$, $\Delta_{\text{beam}} = 0.94\, r = 17.954''$, $r_{\text{btop}} = 10''$.

The resulting energy ratios are plotted against L_{supp} in Figure 5-19, where dots are color-coded by the value of $L_{\text{supp}} + L_{\text{over}}$. In general, the longer the beam, the smaller the energy ratio. This result supports the idea that the AMD can facilitate directing a significant portion of the reflected stress wave towards the arms of the beam. Additionally, we see that $\mathcal{E}_R$ oscillates as a function of L_{supp}, which indicates that the propagation of the stress wave in the beam depends not only on the total beam length but also, to some degree, on the location of supports.

Since the increase of $L_{\text{supp}} + L_{\text{over}}$ from $85''$ to $98''$ yields only a marginal improvement, we propose to consider using the minimum of the energy ratio $\mathcal{E}_R = 0.451$ achieved at the parameter values $L_{\text{supp}} = 32.178''$, $L_{\text{over}} = 85'' - L_{\text{supp}} = 52.822''$ (corresponding to the lowest red triangle in Figure 5-19). The AMD model geometry for this optimal combination of parameter values is shown in Figure 5-8.

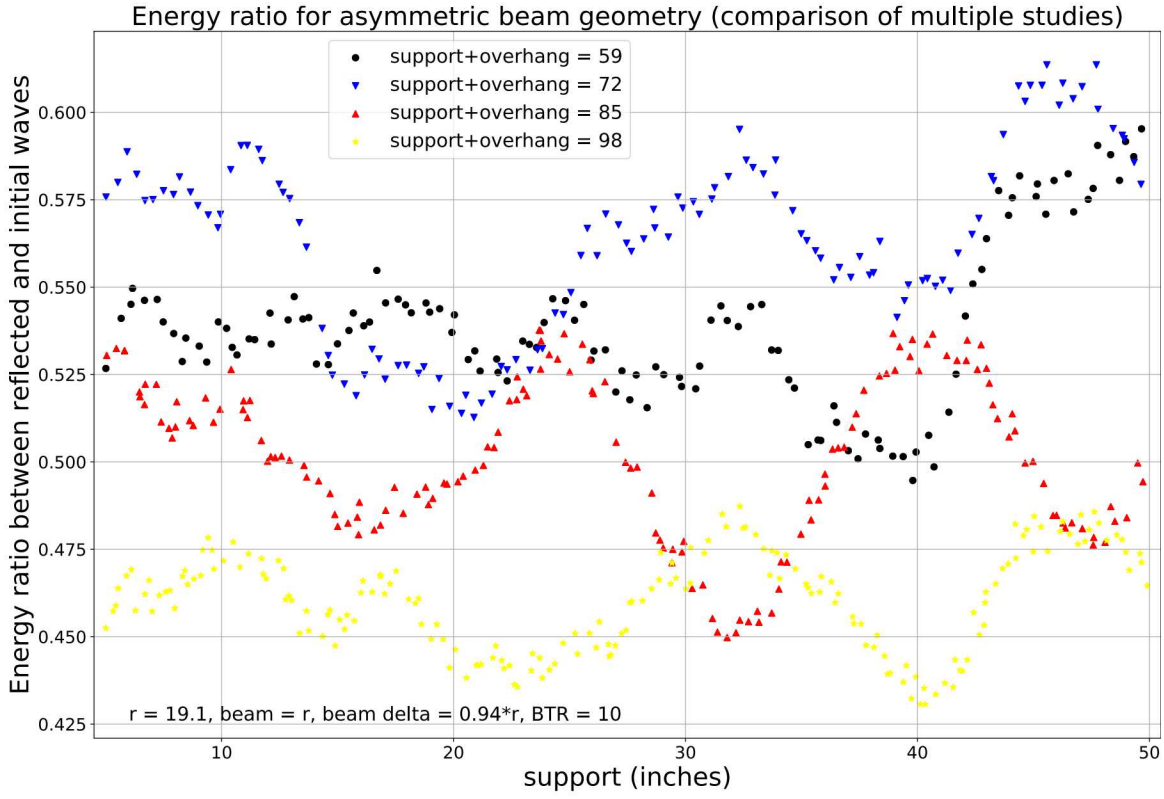

Figure 5-19. Energy ratio $\mathcal{E}_R$ versus L_{supp} for AMD with four different values of $L_{\text{supp}} + L_{\text{over}}$.

5.5.6. *Examples of stress wave propagation*

To illustrate the stress wave propagation in the AMD, Figure 5-20 shows filtered force signals for three combinations of AMD parameter values. The solid black line in Figure 5-20 corresponds to the optimal combination of parameter values described in section 5.5.5 and illustrated in Figure 5-8: $r = 19.1''$, $L_{\text{beam}} = r = 19.1''$, $L_{\text{supp}} = 32.178''$, $L_{\text{over}} = 85'' - L_{\text{supp}} = 52.822''$, $\Delta_{\text{beam}} = 0.94\, r = 17.954''$, $r_{\text{btop}} = 10''$, leading to $\mathcal{E}_R = 0.451$. This is one of the best results we discovered for the AMD. The dashed blue line corresponds to a combination of parameters leading to $\mathcal{E}_R = 1.042$ (a medium quality result for the AMD), and the dash-dotted red line corresponds to a combination of parameters leading to $\mathcal{E}_R = 1.630$ (a poor quality result for the AMD). While the AMD with the optimal combination of parameter values significantly reduces the amplitude of the reflected wave, the reflection is still not negligible, so further improvements are needed.

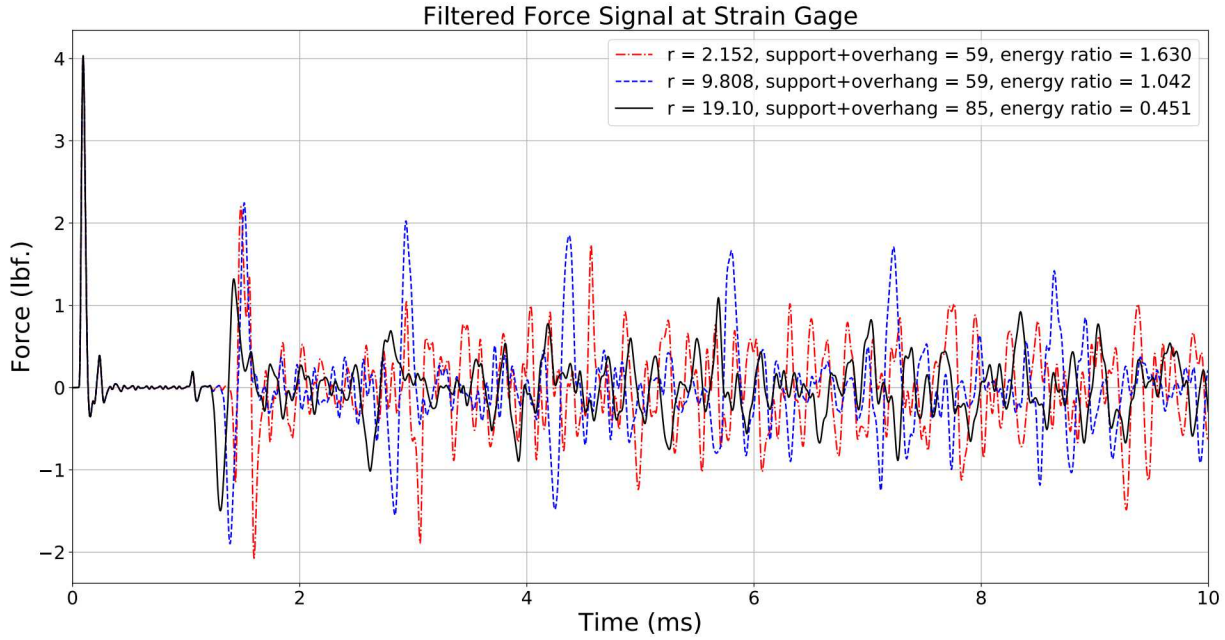

Figure 5-20. Simulated stress wave propagation (filtered force signal) over 10 ms, for AMD with three different sets of parameter values.

6. SUMMARY AND CONCLUSIONS

In the first part of this work, we used finite-element numerical simulations to investigate the possibility of delaying the arrival of the reflected wave at the strain gauge, in order to allow for a longer measurement of the stress–strain response of materials tested in the Dropkinson bar apparatus. For the current Dropkinson bar design with a wave beam attached to the bar, we focused on influencing the WRT by changing the bar–beam connection quality details and properties of the wave beam material. We concluded that either of these changes affects the WRT very insignificantly, due to a reflection that always occurs at the bar–beam boundary. We also studied how the WRT is affected by varying the parameters of an alternative, monolithic design of the bar-and-beam system. In this case, a partial reflection of the stress wave occurs at a point where the bar geometry changes (resulting in the respective change of the impedance). Based on these observations, our final conclusion is that, given a fixed total length of the bar, it is impossible to significantly extend the WRT.

In the second part of this work, we focused instead on trying to minimize the energy of the reflected stress waves circulating up and down through the bar over a period of 10 ms. We found that the ratio of energies between the reflected wave (from its start time to 10 ms) and the initial wave can vary significantly depending on various system parameters.

First, we computed the energy ratio for each of the 18 variants of the bar–beam connection, characterized by the use of either "Tied" (welded or securely threaded) or "Frictional" (sliding) connection fixity at five joints (Bar/Nut Plate, Bar/Nut, Nut Plate/Nut, Nut Plate/Beam, and Bar/Beam). The obtained results demonstrate that the energy of the reflected wave can be significantly influenced by the connection fixities. In particular, four variants for which all three connections to the bar (Bar/Nut Plate, Bar/Nut, and Bar/Beam) are frictional, exhibit very high energy ratio values (> 4.2), due to almost complete reflection of the stress wave from the top end of the bar. This happens due to the fact that in these configurations nearly no load transfer occurs between the bar and the wave beam. On the other hand, some connection variants perform much better in reducing the reflection of the stress wave at the bar–beam boundary. The smallest energy ratio value (1.557) is obtained for variant 9 (FTTFF) and the second smallest value (1.639) for variant 11 (FTFFF), thus providing an improvement compared to the value of 2.160 obtained for variant 0 (TTTTF) implemented in the current experimental setup.

Second, we computed the energy ratio for hundreds of alternative wave beam materials, with varying values of the density and Young's modulus (up to two orders of magnitude larger or smaller than those of AISI 4140). For these hypothetical materials the value of c_{factor} (the ratio of the sound velocity c in the material to that in AISI 4140) varied in the range from 0.01 to 80. For connection variant 0, we observed energy ratio values varying from approximately 0.935 to approximately 4.3, depending on the material properties. The energy ratio increases with c_{factor} as the latter grows from about 0.1 to 10, but stays in a relatively tight range (indicative of a saturation) for $c_{\text{factor}} < 0.1$ and $c_{\text{factor}} > 10$. Additionally, a spread between energy ratio values obtained for materials with the same value of c_{factor} is explained by the difference in the respective values of Z_{factor} (the ratio of the impedance Z in the material to that in AISI 4140). Based on these results, we concluded that the key property of the wave beam material that determines the energy of the reflected wave is the sound velocity but the impedance also plays an important role. When both the wave beam material properties and the connection fixities are varied, the smallest energy ratio value (0.773) is obtained for variant 17 (TTTTT) and the second smallest value (0.821) for variant 4 (TFTTF).

Finally, we investigated the dependence of the energy ratio on parameters of an asymmetric monolithic design of the bar-and-beam system. Two key features of this design are (1) a gradual change of

the bar width (accompanied by a proportionally gradual change of the impedance), resulting in a very weak partial reflection, and (2) a different thickness of the beam's left and right halves, which can produce a destructive interference between the waves reflected down from the left and right parts of the top surface of the beam and thereby direct a significant portion of the reflected wave towards the beam's arms. For an optimal combination of AMD parameter values, we found an energy ratio value of 0.451. Compared to the current Dropkinson bar design, this optimal value is by about 42% smaller than the best value (0.773) obtained by varying both the wave beam material properties and the connection fixities, by about 52% smaller than the best value (0.935) obtained by varying only the connection fixities, and by almost an order of magnitude smaller than the value (4.286) obtained for the worst connection variant.

Looking into the future, we can recommend a number of improvements based on the results of this research. The simplest modification is to change the connection fixities from the currently used variant 0 (TTTTF) to variant 9 (FTTFF), which involves changing the Bar/Nut Plate and Nut Plate/Beam connections from Tied to Frictional. This would result in a modest improvement of the energy ratio from 2.160 to 1.557. A more complicated modification would involve fine-tuning the geometry and material of the wave beam in such a way that the frequency response and effective impedance approach the optimized values identified in this study, thereby minimizing the reflected wave's energy. The analysis of these wave beam characteristics was not performed in the present study but could be the subject of a future work. Furthermore, a future investigation of possibilities offered by a monolithic design of the bar-and-beam system can be useful in a longer perspective. One possible direction for future research could include investigating a combination of a monolithic design (resulting in a better deflection of the reflected wave to the beam's arms) and a wave beam attachment (resulting in a better dissipation of the deflected part of the wave). Another possibility is a monolithic design with a periodic bar geometry, with the goal of producing a destructive interference of multiple reflected waves at the strain gauge location.

To summarize, the primary takeaways for users of the existing Dropkinson bar configuration are:

1. With a limited bar length, it is difficult to appreciably extend the first wave reflection time, even with the addition of the wave beam.
2. The wave beam is effective at reducing the reflected wave magnitudes, though they remain significant.
3. In order to minimize reflected wave energy, the most important considerations of the bar-beam connection are (1) ensuring that the Nut Plate & Nut are securely connected, and a (2) loose/frictional connection between the Nut Plate & Wave Beam.
4. It is likely possible to further reduce reflected wave energy with additional design optimization of the wave beam, either as a separate component or monolithic with the Dropkinson bar.
5. Effective stiffness and impedance are critical quantities in the design of an effective wave beam.

REFERENCES

[1] B. Hopkinson, "A method of measuring the pressure produced in the detonation of high explosives or by the impact of bullets," Proc. R. Soc. Lond. A, 89(612), 411–413 (1914). https://doi.org/10.1098/rspa.1914.0008.

[2] H. Kolsky, "An investigation of the mechanical properties of materials at very high rates of loading," Proc. Phys. Soc. B, 62(11), 676–700 (1949). https://doi.org/10.1088/0370-1301/62/11/302.

[3] W. Chen and B. Song, *Split Hopkinson (Kolsky) Bar: Design, Testing and Applications* (Springer, Boston, MA, 2011). https://doi.org/10.1007/978-1-4419-7982-7.

[4] B. Song, B. Sanborn, J. Heister, R. Everett, T. Martinez, G. Groves, E. Johnson, D. Kenney, M. Knight, and M. Spletzer, "Development of "Dropkinson" bar for intermediate strain-rate testing," in J. Kimberley, L. E. Lamberson, and S. Mates (eds.), *Dynamic Behavior of Materials*, vol. 1, pp. 81–83 (Springer, Cham, Switzerland, 2009). https://doi.org/10.1007/978-3-319-95089-1_12.

[5] *Dropkinson Bar*. https://ip.sandia.gov/technology.do/techID=191.

[6] *Sierra, Sandia's engineering mechanics simulation code suite*. https://sierradist.sandia.gov.

[7] Y. Li, E. Ngo, and B. Song, "A novel design of guiding stress wave propagation," J. Dynamic Behavior Mater. (2020). https://doi.org/10.1007/s40870-020-00253-9.

[8] L.-l. Wang, *Foundations of Stress Waves* (Elsevier, Oxford, UK, 2007), ch. 1. https://doi.org/10.1016/B978-008044494-9/50001-9.

[9] M. D. Schwartz, *The Physics of Waves. Lecture Notes*. "Lecture 9: Reflection, Transmission and Impedance" (2016). http://users.physics.harvard.edu/~schwartz/15cFiles/Lecture9-Impedance.pdf.

DISTRIBUTION

Email—Internal

Name	Org.	Sandia Email Address
Lauren Beghini	08752	llbeghi@sandia.gov
Janine Bennett	08759	jcbenne@sandia.gov
Darcie Farrow	01528	dfarrow@sandia.gov
Colin Loeffler	01528	cloeffl@sandia.gov
Stacy Nelson	08752	smnelso@sandia.gov
Jakob Ostien	08363	jtostie@sandia.gov
Brett Sanborn	01528	bsanbor@sandia.gov
Bo Song	01528	bsong@sandia.gov
Brian Werner	08363	btwerne@sandia.gov
Technical Library	01977	sanddocs@sandia.gov

This page left blank

Sandia National Laboratories

Sandia National Laboratories is a multimission laboratory managed and operated by National Technology & Engineering Solutions of Sandia LLC, a wholly owned subsidiary of Honeywell International Inc. for the U.S. Department of Energy's National Nuclear Security Administration under contract DE-NA0003525.